

Galaxy growth by merging in the nearby universe

Tao Jiang¹, David W. Hogg^{1,2,3}, Michael R. Blanton¹

ABSTRACT

We measure the mass growth rate by merging for a wide range of galaxy types. We present the small-scale ($0.014 < r < 11 h_{70}^{-1}$ Mpc) projected cross-correlation functions $w(r_p)$ of galaxy subsamples from the spectroscopic sample of the NYU VAGC (5×10^5 galaxies of redshifts $0.03 < z < 0.15$) with galaxy subsamples from the SDSS imaging (4×10^7 galaxies). We use smooth fits to de-project the two-dimensional functions $w(r_p)$ to obtain smooth three-dimensional real-space cross-correlation functions $\xi(r)$ for each of several spectroscopic subsamples with each of several imaging subsamples. Because close pairs are expected to merge, the three-space functions and dynamical evolution time estimates provide galaxy accretion rates. We find that the accretion onto massive blue galaxies and onto red galaxies is dominated by red companions, and that onto small-mass blue galaxies, red and blue galaxies make comparable contributions. We integrate over all types of companions and find that at fixed stellar mass, the total fractional accretion rates onto red galaxies ($\sim 3 h_{70}$ percent per Gyr) is greater than that onto blue galaxies ($\sim 1 h_{70}$ percent per Gyr). These rates are almost certainly over-estimates because we have assumed that all close pairs merge as quickly as the merger time that we used. One conclusion of this work is that if the total growth of red galaxies from $z = 1$ to $z = 0$ is mainly due to merging, the merger rates must have been higher in the past.

Subject headings: cosmology: observations — galaxies: evolution — galaxies: fundamental parameters — galaxies: interactions — galaxies: general — methods: statistical

¹ Center for Cosmology and Particle Physics, Department of Physics, New York University, 4 Washington Pl, New York, NY 10003

² To whom correspondence should be addressed: david.hogg@nyu.edu

³ Max-Planck-Institut für Astronomie, Königstuhl 17, D-69117 Heidelberg, Germany

1. INTRODUCTION

The galaxy mergers may play an important role in the evolution of the galaxies. In the color-magnitude space, galaxies are separated into two distinct regions: (1) the ‘red sequence’: the ‘early-type’, red galaxies ; (2) the ‘blue cloud’ or ‘blue sequence’: the ‘late-type’, blue galaxies with strong ongoing star formation (Strateva et al. 2001; Blanton et al. 2003b). Some recent studies in the high-redshift ($z \sim 1$) universe find that the early-type galaxy population is growing over time (Bell et al. 2004; Willmer et al. 2006; Blanton 2006; Brown et al. 2007; Faber et al. 2007; Zhu et al. 2011), which is also found at very high ($z \sim 2$) redshift (Daddi et al. 2005; Trujillo et al. 2007; Longhetti et al. 2007; Toft et al. 2007; Conselice et al. 2007; Cimatti et al. 2008; van Dokkum et al. 2008; Saracco et al. 2009). In numerical simulations, some studies show us that major mergers of intermediate-stellar-mass late-type galaxies maybe play an important role in the growth of the intermediate-stellar-mass early type galaxies (Barnes & Hernquist 1996; Naab & Burkert 2003). However, the massive early type galaxies may grow in a different way (Naab & Burkert 2003). Some recent studies show us that ‘dry mergers’ - the mergers between early-type galaxies - might play an important role in the growth of massive early-type galaxies (Bell et al. 2006b; van Dokkum 2005; Masjedi et al. 2008).

There are a lot of studies that estimate the merger rate among galaxies. These studies can be separated into two general categories. The studies in the first category count the ‘pre-merger’ close pairs and convert the ‘pre-merger’ pairs to a merger rate (*e.g.*, Zepf & Koo 1989; Carlberg et al. 1994, 2000; Carlberg et al. 2000; Patton et al. 1997, 2000; van Dokkum et al. 1999; Lin et al. 2004; Bell et al. 2005; Bell et al. 2006a; Kartaltepe et al. 2007; Masjedi et al. 2006, 2008; Patton & Atfield 2008; Kitzbichler & White 2008; Bundy et al. 2009; De Propris et al. 2007; Lin et al. 2008; de Ravel et al. 2009; De Propris et al. 2010; Robaina et al. 2010). The studies in the second category count the ‘post-merger’ galaxies which have recently experienced at least one merger event. These ‘post-merger’ galaxies are chosen by some observable special properties caused by merging. An example might be by star formation indicators of ‘post-merger’ galaxies (Quintero et al. 2004) or by morphological signatures caused by merger events (Abraham et al. 1996; Conselice et al. 2003; van Dokkum 2005; Lotz et al. 2006; De Propris et al. 2007; Lotz et al. 2008; Conselice et al. 2009).

Our work builds on the earlier works of Masjedi et al. (2006, 2008), which have found previously that luminous red galaxies (LRGs) are growing on average by less than $2 h_{70}$ percent per Gyr from merger activity at redshifts $0.16 < z < 0.30$ (Masjedi et al. 2008). In this paper, we consider both red and blue galaxies. We use the previous technique for measuring the close pairs (Masjedi et al. 2008) on NYU VAGC Spectroscopic Sample and SDSS Imaging Sample, and extend this type of analysis beyond luminous red galaxies (LRGs) to a wide range of

galaxies in both stellar mass and color.

The primary uncertainty in turning a deprojected three-dimensional cross-correlation function at small scales into a merger rate is in estimating the mean time for two galaxies to merge as a function of stellar mass and separation. There are different estimates of merger timescale: free-fall time, orbital time, and dynamical friction time (*e.g.*, Binney & Tremaine 1987; Boylan-Kolchin & Ma 2007; Conroy et al. 2007; Kitzbichler & White 2008; Bundy et al. 2009; Lotz et al. 2010). In this paper, we will use an approximation to the two kinds of merger times under the assumption of Kitzbichler & White (2008) and Binney & Tremaine (1987) as our standard estimate. Both of these times are likely to be an under-estimate of the mean merger time, because some close pairs will not merge at all. Any under-estimate of the merger time leads to an over-estimate of the growth rate.

Throughout this paper, all magnitudes are AB, all apparent magnitudes are model Mag, all masses are stellar masses (in units of $h_{70}^{-2} M_{\odot}$), all velocities are in units of km s^{-1} , all radii of galaxies are r_{90} which contain 90 percent of the Petrosian flux (Blanton et al. 2003b; Blanton & Moustakas 2009), and all volumes and distances are comoving, calculated for a cosmological world model with $(\Omega_m, \Omega_{\lambda}) = (0.3, 0.7)$ and Hubble constant $H_0 \equiv 70 h_{70} \text{ km s}^{-1} \text{ Mpc}^{-1}$.

2. DATA

We use the NYU Value-Added Galaxy Catalog (VAGC) V7.2 data (Blanton et al. 2005), which is built from SDSS data, as our source of spectroscopic data. We use all the SDSS imaging data as our source for cross-correlation samples. The SDSS is a survey of about 10^4 square degrees (Fukugita et al. 1996; Gunn et al. 1998; Gunn et al. 2006; York et al. 1999; York & SDSS Collaboration 2001; Stoughton et al. 2002; Abazajian et al. 2003; Abazajian et al. 2004).

2.1. Spectroscopic Subsample

Our spectroscopic sample is drawn from NYU VAGC V7.2 data. We removed galaxies with apparent magnitudes $r < 14$ mag, because SDSS photometric catalog missed many luminous galaxies nearby (Zhu et al. 2010). Our spectroscopic sample contains about 8.6×10^5 main galaxies, of which about 5×10^5 SDSS Main Samples galaxies (Strauss et al. 2002) are in the redshift range $0.03 < z < 0.15$ (see Figure 1) with apparent magnitudes $r < 17.77$. We cut the redshift at $z < 0.15$, because we want to avoid all quasars, and we cut the

redshift at $z > 0.03$, because we want to avoid all stars. We use the code `sdss_kcorrect` (Blanton & Roweis 2007) to calculate the K -corrected absolute magnitude at $z = 0.1$ and stellar mass for each. We cut this sample into 10 subsamples by stellar mass and make sure that in each subsamples the number of galaxies is the same. After that, we cut them into red and blue using the cut (Hogg et al. 2004):

$$^{0.1}g - ^{0.1}r = 0.0625 \times \log(M) + 0.15 \quad (1)$$

where M is the stellar mass. These cut the spectroscopic sample into 20 spectroscopic subsamples; we call these subsamples \mathbb{D}_s (see Figure 2). For the red spectroscopic subsamples, we name the smallest stellar-mass subsample ‘red0’, then name the second smallest stellar-mass subsample ‘red1’, and so on, so the largest stellar-mass subsample is named ‘red9’, and the same for the blue spectroscopic subsamples. Figures 3 and 4 show the number density of galaxies of the 18 spectroscopic subsamples as a function of redshift. The red0 and blue0 subsamples are low in number density, and highly affected by survey selection effects, so we do not use them further. We can see that blue8, blue9 and red9 appear to rise in number density with redshift, this is because we removed galaxies with apparent magnitudes $r < 14$ mag.

The SDSS suffers from the ‘fiber collision’: the angular separation between any two spectroscopic targets must be larger than 55 arcsec. There are about ~ 9 percent of target galaxies which do not have redshifts because of this fiber collision. Using the counting-close-pairs technique of Masjedi et al. (2008), the fiber collision will not affect our pair counts directly under the approximation that the unmeasured galaxies and the measured galaxies are similar in cross-correlation with fainter galaxies.

Following the technique of Masjedi et al. (2008), we estimate the weight p_j that accounts the spectroscopic incompleteness from fiber collisions effects, and the weight f_j that accounts the spectroscopic incompleteness from all other selection effects in SDSS. For each galaxy j in the spectroscopic subsample, we calculate p_j by using a two-dimensional ‘FOF’ (friends-of-friends) grouping algorithm on our main galaxies targets with a 55-arcsec linking length:

$$p_j = \frac{N_s^j}{N_{total}^j} \quad (2)$$

Where N_{total}^j is the total number of main galaxies targets in group j , N_s^j is the number of main galaxies with redshift measurement in group j , and the group which contains galaxy j , is called group j . All $p_j \geq 1$ because $N_{total}^j \geq N_s^j$.

For each spectroscopic subsample \mathbb{D}_s , we create a random spectroscopic subsample \mathbb{R}_s which is 10 times large as \mathbb{D}_s . For each galaxy in \mathbb{D}_s , we created 10 galaxies with the exactly

same redshift but angular position taken from the two-dimensional random sample. Thus, we create a large random spectroscopic subsample \mathbb{R}_s which match the redshift distribution of \mathbb{D}_s , and \mathbb{R}_s is isotropic within the SDSS survey region.

The SDSS survey region is separated into small unique region ‘sector’. For each random point j in \mathbb{R}_s :

$$f_j = \frac{1}{F_j} \quad (3)$$

Where F_j is the fraction of main galaxy targets for which a classification was obtained in the object’s sector (in our NYU-VAGC spectroscopic sample, the average F_j is $\bar{F} \approx 0.91$).

Our correction of fiber collisions is: we weight the target j in spectroscopic subsample \mathbb{D}_s as p_j and weight the target j in random spectroscopic subsample \mathbb{R}_s as f_j . From the previous work (Masjedi et al. 2006), we know that this correction will improve in the spectroscopic incompleteness due to fiber collisions at very small separations ($w(r_p) < 100h_{70}^{-1}$ kpc). In Section 4.1, we will compare our result with the result of Zehavi et al. (2010), and will show that our result with this correction of fiber collisions fits better than the result without this correction of fiber collisions.

For each spectroscopic sample ‘s’ (\mathbb{D}_s or \mathbb{R}_s), in which there are N_s spectroscopic galaxies, we divide it into the 50 bins by lines of constant dec, so that there are $N_s/50$ spectroscopic galaxies in each bin. Then we resample them into 50 leave-one-out resampling samples, so that there are $49/50 \times N_s$ spectroscopic galaxies in each sample. We call them the ‘50 resampling samples’, with which we can calculate our jackknife resampling covariance matrix.

2.2. Imaging Subsamples

For our imaging data, we use a sample drawn from the full SDSS imaging catalog in which there are about 4×10^7 galaxies. We include from the SDSS imaging sample only galaxies with apparent magnitude $14 < r < 21.5$ mag, and apparent color $-0.5 < [g - r] < 2$ mag, see Figures 5 and 6. We removed galaxies with apparent magnitudes $r < 14$ mag for the same reason with our spectroscopic sample. We also removed galaxies with apparent magnitudes $r > 21.5$ mag, because these galaxies are not well observed and their observed number density is much lower than their real number density. Please note that this cut will affect our minor merger near mass ratio 1 : 100. Similar to the spectroscopic sample, we create a random imaging sample \mathbb{R}_i as large as possible. The angular positions of galaxies in \mathbb{R}_i are taken from the two-dimensional random sample. So \mathbb{R}_i is isotropic within the SDSS survey region.

2.3. Grid Method K -corrections for galaxies from the imaging sample

We also need to compute the stellar mass of galaxies in the imaging subsamples in order to determine the mass ratio, so we want to K -correct galaxies in the imaging subsamples. However, we cannot K -correct individual galaxies in the imaging subsamples once and for all, because we do not have spectroscopic redshifts for them. Each time we consider a pair of galaxies, one from the spectroscopic subsample and one from the imaging subsample, we assign the spectroscopic redshift to the galaxy from the imaging sample. This allows us to calculate for each galaxy from the imaging sample in each spectroscopic–imaging pair a temporary K -corrected stellar mass and $[^{0.1}g - ^{0.1}r]$ color for the purposes of that pair. We discard these values and compute new ones when the galaxy from the imaging sample is used in another pair with another galaxy from the spectroscopic sample.

To save time, we take galaxies from the NYU VAGC spectroscopic sample as representative of all galaxy types, and apply the code `sdss_kcorrect` on the galaxies from a grid named ‘B’ of observed r -band magnitude (0.5 mag per bin), $[g - r]$ color (0.1 mag per bin), and redshifts between 0.03 and 0.15 (0.0002 per bin). We saved the mean K -corrected stellar mass M_B and $[^{0.1}g_B - ^{0.1}r_B]$ color in a grid of observed r -band magnitude, $[g - r]$ color, and redshift, also save the mean redshift z_B , mean r_B and mean $[g_B - r_B]$ color, Thereafter we estimated the K -corrected stellar mass and $[^{0.1}g - ^{0.1}r]$ color for a galaxy G in grid B, and the $[g_G - r_G]$ color of galaxy G is between $[g_B - r_B]$ color of grid B and $[g_C - r_C]$ color of grid C which is next to grid B (that means z_B and z_C are the same, and r_B and r_C are the same):

$$\log M_G = \log (M_B \times \frac{(d_L^G)^2}{(d_L^B)^2}) - \frac{r_G - r_B}{2.5} + \frac{(\log M_C - \log M_B) \times ([g_G - r_G] - [g_B - r_B])}{[g_C - r_C] - [g_B - r_B]} \quad (4)$$

$$[^{0.1}g_G - ^{0.1}r_G] = [^{0.1}g_B - ^{0.1}r_B] + [g_G - r_G] - [g_B - r_B] \quad (5)$$

where d_L is the luminosity distance calculated from redshift, and galaxy G is in grid B, so the difference between z_B and z_G is small, similarly, the difference is small between d_L^G and d_L^B , r_b and r_G , $[g_B - r_B]$ and $[g_G - r_G]$. because of these small differences, the equations (4) and (5) can be used. This speeds up the K -correction procedure immensely and only introduces a 12-percent one-sigma error for each galaxy and there is little bias (see Figure 7), so only introduces percent-level errors in the results. We call this ‘Grid Method’ hereafter.

For grids with observed r -band magnitude $r > 17.77$ mag, we cannot get the mean stellar mass and $[^{0.1}g - ^{0.1}r]$ color directly, because there are no galaxies from the spectroscopic sample at observed r -band magnitude $r > 17.77$ mag. In order to estimate the color and stellar mass of the galaxies in grid A with mean observed r -band magnitude $r_A > 17.77$ mag, we find the grid point B that has the nearest mean observed r -band magnitude r_B ($r_B >$

17.77 mag) and has the same observed $[g - r]$ color and the same redshift, also there are at least 10 galaxies from the spectroscopic sample in grid B. Then we estimate M_G and $[^{0.1}g_G - ^{0.1}r_G]$ color of galaxy G in grid A using the equation (4) and (5). If we cannot find a grid B satisfying the conditions, we will leave all the galaxies in grid A empty.

Figure 8 shows the difference between the color estimate using the Grid Method above and the color calculated using the code `sdss_kcorrect`. The one-sigma error for each galaxy is about 0.04 mag and there is little bias (see Figure 8).

2.4. Velocities for merger rate estimates

In this Section, we will estimate the average orbital velocity which will be used to estimate the merger time in Section 3.4. Please note that this approximation will induce a large error in the estimate of merger time, because we assume that all close pairs merge under the following orbital velocity which is not true for close pairs in high velocity-dispersion.

The average orbital velocity for a galaxy from the imaging sample around a more massive red galaxy from the spectroscopic subsample s with average velocity dispersion σ_v is very roughly 1.5 times the velocity dispersion, here we have included the factor of 1.5 to be conservative (Masjedi et al. 2008). We estimate the σ_v with Faber-Jackson relation:

$$\log \sigma_v = a_1 + b_1 \log M_s^{red} \quad (6)$$

where M_s^{red} is the mean stellar mass of the red galaxies from spectroscopic subsample s . We performed a linear fit to the data to obtain $a_1 = -1.588$ and $b_1 = 0.354$ (Figure 9). Please note that the method above will induce a small enough error (< 1 percent) into our final result.

We estimate the average orbital velocity V_c for a galaxy from the imaging sample around a more massive blue galaxy from the spectroscopic subsample s with the Tully-Fisher relation:

$$\log V_c = a_2 + b_2 \log \langle L_I \rangle \quad (7)$$

where $\langle L_I \rangle$ is the mean I-band luminosity of the blue galaxies from spectroscopic subsample s , calculated from $L_I = M/r_I$, where M is the stellar mass of the galaxy and r_I is the I-band mass-to-light ratio of the galaxy calculated from the code `sdss_kcorrect`. We used for this relationship $a_2 = -0.835$ and $b_2 = 0.291$ (Courteau et al. 2007).

Table 1 provides this information for all 20 spectroscopic subsamples.

3. Method

For each spectroscopic subsample \mathbb{D}_s , we cut the imaging sample into 16 subsamples by stellar mass: $10^{-\frac{j}{8}} < M_i^G/M_s < 10^{-\frac{j-1}{8}}$, where M_i^G is the stellar mass of a galaxy from the imaging sample, calculated by the Grid Method using the redshift of the spectroscopic galaxy, and M_s is the mean stellar mass of the galaxies from spectroscopic subsample s , and j is an integer $1 \leq j \leq 16$, that means a mass ratio of 1 : 1 to 1 : 100 is covered. After that, we cut them into red and blue using equation (1) by $[^{0.1}g - ^{0.1}r]$ color calculated by Grid Method. For each spectroscopic subsample \mathbb{D}_s , these cut the imaging sample into 32 imaging subsamples \mathbb{D}_i .

In this section, we will show our method to estimate the merger rate between galaxies in spectroscopic subsample \mathbb{D}_s and galaxies in imaging subsample \mathbb{D}_i : (1) we estimate the projected two-dimensional cross-correlation function $w_{si}(r_p)$ as a function of tangential projected separation r_p ; (2) we de-project the smooth fit for the cross-correlation function $w_{si}(r_p)$ to obtain the three-dimensional real-space cross-correlation function $\xi_{si}(r)$ as a function of real-space separation r ; (3) we estimate the merger rate using $\xi_{si}(r)$ and our two kinds of merger times (Binney & Tremaine 1987; Kitzbichler & White 2008). In addition, we will also discuss our method of photometry correction.

3.1. Projected cross-correlation function

To estimate the $w_{si}(r_p)$ between spectroscopic subsample \mathbb{D}_s and imaging subsample \mathbb{D}_i , we can integrate $\xi_{si}(r)$ along the line of sight (*e.g.*, Davis & Peebles 1983):

$$w_{si}(r_p) = 2 \int_0^\infty dy \xi_{si} [(r_p^2 + y^2)^{1/2}] \quad (8)$$

This integral is dominated by scales $y \lesssim r_p$.

Using the previous approach (Masjedi et al. 2006, 2008), we estimate not $w_{si}(r_p)$ but $\rho_i w_{si}(r_p)$, where ρ_i is the average comoving three-dimensional stellar mass density of the imaging subsample i :

$$\rho_i w_{si}(r_p) = \frac{D_s D_i}{D_s R_i} - \frac{R_s D_i}{R_s R_i} \quad (9)$$

Where D_s and D_i represent the spectroscopic and imaging data subsamples, and R_s and R_i represent the spectroscopic and imaging random subsamples. Similar to the previous method (Masjedi et al. 2006, 2008), equation (9) measures the mass-weighted abundance of pairs ($\frac{D_s D_i}{D_s R_i}$) and subtracts the mean background level ($\frac{R_s D_i}{R_s R_i}$). This method has been well tested in Masjedi et al. (2006).

In detail, the factors are defined as follows:

$$D_s D_i = \frac{\sum_{j \in \mathbb{D}_s \mathbb{D}_i} p_j}{\sum_{j \in \mathbb{D}_s} p_j} \quad (10)$$

where the top sum counts the weighted pairs j of galaxies from \mathbb{D}_s and \mathbb{D}_i separated by tangential projected distance r_p , and the bottom sum is over galaxies j from \mathbb{D}_s . This factor $D_s D_i$ is dimensionless.

$$D_s R_i = \frac{\sum_{j \in \mathbb{D}_s \mathbb{R}_i} p_j}{\sum_{j \in \mathbb{D}_s} p_j \left[\frac{d\Omega}{dA} \right]_j \frac{dM}{d\Omega}} \quad (11)$$

where the top sum counts the weighted pairs j of galaxies from \mathbb{D}_s and \mathbb{R}_i separated by tangential projected distance r_p . In the bottom, $\left(\frac{d\Omega}{dA} \right)_j$ is the inverse square of the transverse comoving distance (Hogg 1999) to galaxy j from \mathbb{D}_s , and $\frac{dM}{d\Omega}$ is calculated by $\frac{dM}{d\Omega} = \frac{dN}{d\Omega} \times M_i$, where $\frac{dN}{d\Omega}$ is the two-dimensional number density of \mathbb{R}_i per solid angle, and

$$M_i = M_s \times 10^{-\frac{j-0.5}{8}} \quad (12)$$

where M_i is the mean stellar mass of galaxies from the imaging subsample i , and j is an integer $1 \leq j \leq 16$. Then $\left(\frac{d\Omega}{dA} \right)_j \times \frac{dM}{d\Omega}$ represents the average stellar mass of galaxies in \mathbb{R}_i per unit comoving area around each galaxy from \mathbb{D}_s . This factor $D_s R_i$ has dimensions of comoving area divided by stellar mass.

$$R_s D_i = \frac{\sum_{j \in \mathbb{R}_s \mathbb{D}_i} f_j}{\sum_{j \in \mathbb{R}_s} f_j} \quad (13)$$

this is similar to equation (10), but \mathbb{R}_s represents now the random catalog mentioned in Section 2.1. This factor $R_s D_i$ is dimensionless.

$$R_s R_i = \frac{\sum_{j \in \mathbb{R}_s \mathbb{R}_i} f_j}{\sum_{j \in \mathbb{R}_s} f_j \left[\frac{d\Omega}{dA} \right]_j \frac{dM}{d\Omega}} \quad (14)$$

this is similar to equation (11), but \mathbb{R}_s represents now the random catalog mentioned in Section 2.1. This factor $R_s R_i$ has dimensions of comoving area divided by stellar mass.

For some experiments, we need to estimate $n_i w_{si}(r_p)$, where n_i is the average comoving three-dimensional number density of the imaging subsample i . We estimate this by the following estimation:

$$n_i w_{si}(r_p) = \frac{D_s D_i}{[D_s R_i]_N} - \frac{R_s D_i}{[R_s R_i]_N} \quad (15)$$

For $D_s D_i$ and $R_s D_i$, it is as the same as equation (10) and equation (13). For $[D_s R_i]_N$ and $[R_s R_i]_N$:

$$[D_s R_i]_N = \frac{\sum_{j \in \mathbb{D}_s \mathbb{R}_i} p_j}{\sum_{j \in \mathbb{D}_s} p_j \left[\frac{d\Omega}{dA} \right]_j \frac{dN}{d\Omega}} \quad (16)$$

this is similar to equation (11), but $\frac{dN}{d\Omega}$ is the two-dimensional number density of the random imaging catalog per solid angle. This factor $D_s R_i$ has dimensions of comoving area.

$$[R_s R_i]_N = \frac{\sum_{j \in \mathbb{R}_s \mathbb{R}_i} f_j}{\sum_{j \in \mathbb{R}_s} f_j \left[\frac{d\Omega}{dA} \right]_j \frac{dN}{d\Omega}} \quad (17)$$

this is similar to equation (14). This factor $R_s R_i$ has dimensions of comoving area.

In range of our interest $0.0149 < r_p < 11.9 h_{70}^{-1}$ Mpc, we bin the spectroscopic-imaging pairs counting by the comoving projected separation r_p of the pair where $r_p = r_k = 0.0149 \times 10^{k/5} h_{70}^{-1}$ Mpc and k is an integer $0 \leq k \leq 14$. We have already discussed how to bin the spectroscopic sample \mathbb{D}_s and the imaging sample \mathbb{D}_i in Section 2. We have combined the 16 stellar mass bins into 4 to simplify the figures. Figures 10 through 13 show the results of our measurements of $\rho_i w_{si}(r_p)$.

The uncertainties on the results shown in these figures are estimated using jackknife resampling covariance matrix with 50 resampling samples (see Section 2.1), please note that all the error bars in our graphs only come from the jackknife resampling covariance matrix (there are some other errors like the error of the color and stellar mass estimated by the Grid Method, and so on). On hundreds of kiloparsec scales, the error bars for each subsample are smallest. On smaller scales, the error bars become larger because of the ‘shot noise’: the smaller the separations, the fewer the pair counts. On larger scales ($> 1 h_{70}^{-1}$ Mpc), the error bars become larger because there are more and more interlopers on larger scales which means that the background subtraction is more noisy.

Figures 10 through 13 show that $n_i w_{si}(r_p)$ is a complex function of r_p . However, on very small scales - tens of kiloparsec scales, we assume that $n_i w_{si}(r_p)$ scales (something) like

r_p^{-1} (Masjedi et al. 2006, 2008). We fit each set of $w_{si}(r_k)$ data with the smooth model:

$$\tilde{w}(r_p) = w_0 \left[1 + \frac{r_p}{r_c} \right]^\gamma \left[\frac{r_p}{r_c} \right]^{-1} \quad (18)$$

by minimizing

$$\chi_{si}^2 \equiv \sum_k \frac{(\rho_i \tilde{w}(r_k) - \rho_i w_{si}(r_k))^2}{\rho_i^2 \sigma_{si}(r_k)^2} \quad (19)$$

We choose $r_c = 12.5 r_{90}$ for Figure 10 to Figure 13 (where r_{90} is the median radii of the galaxies in the corresponding spectroscopic subsamples); then find the γ and $\rho_i w_0$ that minimizes χ_{si}^2 . Figures 10 through 13 show us these fits.

3.2. Photometry Correction

One important issue with all clustering measurements on small scales is possible photometric biases when measuring close pairs. This issue can directly lead to biased flux measurements (Masjedi et al. 2006) and biased color measurements for galaxies, and will indirectly affect stellar masses, k-corrections, etc. This can be due to poor photometry in crowded systems (Patton et al. 2011).

We build our method to correct photometric biases upon the photometry test of Masjedi et al. (2006). In Masjedi et al. (2006), they created fake images of pairs of identical galaxies with separations ranging from 2 to 35 arcsec. These galaxies represent passively evolving LRG galaxies observed at a redshift of $z = 0.3$ with de Vaucouleurs profiles ($n = 4$ Sérsic profiles). Then they placed one such galaxy pair onto RUN 2662 (which has a typical SDSS seeing of about 1 arcsec) of SDSS imaging. After inputting the known info into the mock galaxy images, they processed these images as raw SDSS images using the standard SDSS pipeline, PHOTO, to determine the effect of proximity of galaxies on their measured properties (see plot 1 in Figure 14). At separations larger than 20 arcsec, the Petrosian flux measures 79.5 percent of the input Sérsic flux, which is calculated by three sigma out-layer rejected average. In other words, the Petrosian flux only measures about 80 percent of a galaxy’s light. We are interested in intermediate separations, ($5 < s < 20$ arcsec), in which the fraction of the recovered flux to input flux increases to 83 percent. This increase is likely due to a double counting of the low level diffuse emission from the two galaxies which is being poorly deblended between the two objects.

For pairs of main galaxies, we study two different cases: one for galaxy pairs consisting of two identical galaxies and another with galaxies of different stellar mass. For Case 1, we consider a pair of identical main galaxies with radii of r_{90}^{main} (at redshift $0.03 < z_{main} < 0.15$)

than that of the LRGs r_{90}^{LRG} at redshift $z = 0.3$ (see plot 1 and 2 in Figure 16). We take the following two approximations: (1) If we consider a pair of identical main galaxies which are at the same redshift $z = 0.3$, then the only difference between this pair of main galaxies and the pair of LRGs (see plot 1 in Figure 14) is that the angular radii of the main galaxies is smaller than that of LRGs by a factor of $r_{90}^{main}/r_{90}^{LRG}$. So we compress the result of plot 1 in Figure 14 by a factor of $r_{90}^{main}/r_{90}^{LRG}$ (see plot 2 in Figure 14 as an example) as the effect of proximity of a pair of identical main galaxies. (2) If we consider a pair of LRGs which are at a different redshift $z = z_{main}$, then the only difference between this pair of LRGs and the pair of the LRGs at redshift $z = 0.3$ (see plot 1 in Figure 14) is that the angular radii of this pair of LRGs is larger than that of the LRGs at redshift $z = 0.3$ by a factor of D^{main}/D^{LRG} , where D^{main} is the comoving distance from $z = z_{main}$ to us, and D^{LRG} is the comoving distance from $z = 0.3$ to us. So we stretch the result of plot 1 in Figure 14 by a factor of D^{main}/D^{LRG} (see plot 1 in Figure 15 as an example, and D^{main} at redshift $z = 0.144246$ is nearly half of D^{LRG}) as the effect of proximity of a pair of LRGs at redshift $z = z_{main}$. Combining the above two approximations, the final effect of proximity of a pair of identical main galaxies at a different redshift $z = z_{main} \neq 0.3$, will be stretched by a factor of $r_{90}^{main}/r_{90}^{LRG} \times D^{main}/D^{LRG}$ (see plot 2 Figure 15 as an example). Using this method we correct the flux measurement of our sample on small scales of major merger between main galaxies and we assume that the correction of stellar mass is equal to that of flux. For Case 2, it is based on the above Case 1 but involving the radii r_{90} of the pair of galaxies (r_A and r_B) in our estimation. In plot 2 of Figure 16, we take the third approximation: (3) The flux density from the left galaxy onto the right galaxy is a constant D_A (this approximation lead to a small error comparing to the flux density from the galaxy A onto the galaxy B in plot 3 of Figure 16). We mark the percent increase of flux from the other galaxy as P_{flux} , that of stellar mass as P_{mass} , radius of galaxy A as r_A total flux as F_A and stellar mass as M_A . Then we get the following result:

$$P_{mass} = P_{flux} = \frac{D_A \times \pi r_A^2}{F_A} \quad (20)$$

In plot 3 of Figure 16, we assume that the flux density from the galaxy A onto the galaxy B is equal to D_A and the flux density from galaxy B onto galaxy A is equal to D_B . We mark the percent increase of flux of galaxy B from the galaxy A as P_{flux}^B , that of stellar mass as P_{mass}^B , radius of galaxy B as r_B total flux as F_B , stellar mass as M_B , and the percent increase of flux of galaxy A from the galaxy B as P_{flux}^A , that of stellar mass as P_{mass}^A . Then we get the following results:

$$D_B = D_A \times \frac{F_B}{F_A} = D_A \times \frac{M_B}{M_A} \quad (21)$$

$$P_{mass}^A = P_{flux}^A = \frac{D_B \times \pi r_A^2}{F_A} = P_{mass} \times \frac{M_B}{M_A} \quad (22)$$

$$P_{mass}^B = P_{flux}^B = \frac{D_A \times \pi r_B^2}{F_B} = P_{mass} \times \frac{M_A}{M_B} \times \frac{r_B^2}{r_A^2} \quad (23)$$

Using this result we correct the flux and stellar mass measurements of our sample on small scales of minor merger between main galaxies.

Please note that our photometry correction is overestimated because of the above approximations (1) and (2). In approximations (1) and (2), we assume that the absolute angular scale does not matter; and the only change comes from the ratio of the absolute angular radii of the pair of galaxies to the absolute angular separation of the pair of galaxies. However, we know that absolute angular scale *does* matter: at the same ratio the larger the absolute angular is, the easier the deblending will be. So approximations (1) and (2) will contribute a few percent error in our final result of photometry correction.

After the above photometry correction, we reset our spectroscopic and imaging subsamples to recalculate the $\rho_i w_{si}(r_p)$ using the method in Section 3.1 (see the first and second data points in Figures 10 through 13). Please note that we also apply our photometry correction on the galaxies with no nearby companions, however these galaxies have zero weight in our pair-counting and will not affect our result, because there are no companions near these galaxies during counting pairs. In order to show our method of photometry correction is robust, we double our photometry correction and find that all the percentage difference between the result of our photometry correction and double our photometry correction is below 26 percent for one data point. Then, this data point with 26 percent change will only contribute a few percent error in our final result of the total fractional accretion rate after our fitting curve (see equation (18) and (19)). So, if we assume that the percent error of our photometry correction in flux is 100%, the final effect onto the total fractional accretion rate is at most a few percent.

We use the above method to correct the photometric biases, and we find that our correction due to photometric biases is much smaller than that of Masjedi et al. (2006), because: (1) Main galaxies have smaller radii than LRGs, so it is easier to deblend a pair of main galaxies than a pair of LRGs. (2) Photometry correction of auto-correlation of Masjedi et al. (2006) is larger than that of our cross-correlation, this is because of the difference of the stellar mass cut of spectroscopic/imaging sample between us: for auto-correlation, the stellar mass cut of spectroscopic/imaging sample will be $M_s > M_{threshold}^{lower}$ and $M_i > M_{threshold}^{lower}$, so after photometry correction, the only effect is that some spectroscopic (and imaging) galaxies near $M_{threshold}$ will be cut off from the spectroscopic (and imaging) sample which will decrease the pair-counting. However this is not the only effect on cross-correlation. For cross-correlation, the stellar mass cut of spectroscopic and imaging sample will be $M_{threshold}^{lower} < M_s < M_{threshold}^{upper}$ and $M_i^{lower} < M_i < M_i^{upper}$, so after photometry correction, besides the above effect there

is another effect that some spectroscopic and imaging galaxies which are a little bit above $M_{threshold}^{upper}$ or M_i^{upper} will be counted into the spectroscopic/imaging sample from outside. This effect will increase the pair-counting. Combining the two effects above for cross-correlation, the final photometry correction for cross-correlation will be smaller than that for auto-correlation.

3.3. Three-dimensional statistics

The smooth fit $w(r_p)$ to each projected correlation functions $w_{si}(r_p)$ can be deprojected to get an estimate of the three-dimensional space correlation function $\xi(r)$ by

$$\rho_i \xi(r) = -\frac{1}{\pi} \int_r^\infty dr_p \frac{d[\rho_i w_p(r_p)]}{dr_p} (r_p^2 - r^2)^{-1/2} \quad (24)$$

(*e.g.*, Davis & Peebles 1983), where ρ_i is a constant.

The mean total stellar mass M_i^* of galaxies from a specific imaging subsample i within a given small three-dimensional separation r_{close} around each galaxy from spectroscopic subsample s is:

$$M_i^* = \rho_i \int dV_i [1 + \xi_{si}(r)] = 4\pi \rho_i \int_0^{r_{close}} r^2 dr [1 + \xi_{si}(r)] \quad (25)$$

At small scales, $\xi_{si}(r) \gg 1$, so:

$$M_i^* \approx 4\pi \int_0^{r_{close}} r^2 dr [\rho_i \xi_{si}(r)] \quad (26)$$

From $[\rho_i \xi_{si}(r)]$ we can see that we do not need to measure ρ_i and $w_{si}(r_p)$ separately.

At very small scale ($r_{close} \ll r_c$):

$$M_i^* \approx 4 \rho_i w_0 r_c r_{close} \quad (27)$$

Similarly, the average number N_i^* of galaxies from a specific imaging subsample i within a given small three-dimensional separation r_{close} per galaxy from spectroscopic subsample s at very small scale ($r_{close} \ll r_c$) is:

$$N_i^* \approx 4 n_i w_0 r_c r_{close} \quad (28)$$

3.4. Merger rate

We can estimate the merger rate Γ_i of galaxies from sample i into galaxies from sample s per spectroscopic galaxy per unit time by:

$$\Gamma_i = \frac{N_i^*}{t_{merge,i}} \quad (29)$$

The mean fractional stellar-mass accretion rate of galaxies from spectroscopic subsample s from merging with galaxies from imaging subsample i per unit time is:

$$\left[\frac{d \ln M_s}{dt} \right]_i = \frac{1}{M_s} \left[\frac{d M_s}{dt} \right]_i \approx \frac{M_i^*}{t_{merge,i} M_s} \quad (30)$$

In principle, all merger rate estimates depend on the radius r_{close} inside of which we have counted close pairs. However in this work, we are interested in the instant merger rate estimates, which means that we are interested in the range of $r_{close} \ll r_c$, and this range can be reached using our fit lines. Another reason why we use our fit lines instead of using the data points at very small scales, is that the error bars due to the shot noise for each subsample are very large. From these fit lines in Figures 10 through 13 we know, over the range of interest ($r_{close} \ll r_c$) $w_{si}(r_p)$ scales like r_p^{-1} , $\xi(r)$ scales like r^{-2} , N_i^* and M_i^* scale (something) like r_{close} . Similarly, both of the time-scales ($t_{KW,i}$ and $t_{BT,i}$) scale like r_{close} . For this reason, at $r_{close} \ll r_c$ the above merger and accretion rates do *not* depend strongly on r_{close} .

In this work, we use these two merger time estimates: $t_{BT,i}$ from Binney & Tremaine (1987) and $t_{KW,i}$ from Kitzbichler & White (2008). Both of them depend on the orbital merger time t_{orbit} :

$$t_{orbit}^{red} = \frac{2 \pi r_{close}}{1.5 \sigma_v} \quad (31)$$

Where $1.5 \sigma_v$ is the average orbital velocity for a galaxy from the imaging sample orbiting a more massive red galaxy from the spectroscopic sample with velocity dispersion σ_v , see equation (6). Similarly, the orbital merger time for a galaxy from the imaging sample merged into a more massive blue galaxy from the spectroscopic subsample is

$$t_{orbit}^{blue} = \frac{2 \pi r_{close}}{V_c} \quad (32)$$

Where V_c is the average orbital velocity for a galaxy from the imaging sample around a more massive blue galaxy from the spectroscopic sample, see equation (6).

For the assumption of $t_{KW,i}$ from Kitzbichler & White (2008), the approximation becomes

$$t_{KW,i} = t_{orbit} \left[\frac{M_s}{M_i} \right]^{0.3} \quad (33)$$

where we assume $M_s > M_i$. The solid lines in Figures 17 and 18 as a function of the mass ratio M_i/M_s show the merger rate under assumption of Kitzbichler & White (2008). The total fractional accretion rate is the area under each curve.

For the assumption of $t_{BT,i}$ from Binney & Tremaine (1987), $t_{BT,i}$ is longer than the orbital merger time t_{orbit} by a factor roughly equal to the ratio of the stellar masses (Binney & Tremaine 1987; Masjedi et al. 2008):

$$t_{BT,i} = t_{orbit} \frac{M_s}{M_i} \quad (34)$$

where we assumed $M_s > M_i$. The dashed lines in Figures 17 and 18 as a function of the mass ratio M_i/M_s show the merger rate under assumption of all possible mergers taking place within one dynamical friction time (Binney & Tremaine 1987; Masjedi et al. 2008), and the total fractional accretion rate is the area under the curves.

We integrate the mass accretion rate from mergers over all imaging subsamples and find the total fractional accretion rate ($h_{70} \text{ Gyr}^{-1}$) of all the main galaxies. This is shown with solid lines (for $t_{KW,i}$) and dashed lines (for $t_{BT,i}$) in Figure 19. Please note that the errors from merger time are shown in this figure.

Table 2 shows the total fractional accretion rates of all the 20 spectroscopic subsamples for both the assumption of $t_{merge,i} = t_{KW,i}$ and the assumption of $t_{merge,i} = t_{BT,i}$.

4. Comparison to Previous Work

4.1. Comparison to previous clustering results

We estimate not $w_p(r_p)$ but $n_i w_p(r_p)$. In order to estimate $w_p(r_p)$ and compare with previous results, we need to estimate n_i :

$$w_p(r_p) = \frac{n_i w_p(r_p)}{n_i} \quad (35)$$

It is difficult within the SDSS data to precisely measure the real-space number densities for the imaging subsamples with stellar masses $M_i < 6 \times 10^9 h_{70}^{-2} M_\odot$, because there is only good spectroscopic information about bright members of the imaging sample. However, for galaxies with stellar masses $M_i > 6 \times 10^9 h_{70}^{-2} M_\odot$, the real-space number density n_i for the imaging subsample i is measurable:

$$n_i = \frac{n_i^s}{\bar{F}} \quad (36)$$

where n_i^s is the average real-space number density for the corresponding spectroscopic subsample s within its volume limit, and \bar{F} is the mean fraction of Main targets for which

a classification was obtained in the object’s sector, for NYU-VAGC spectroscopic sample $\bar{F} \approx 0.91$. We assume that n_i is non-evolving over the redshift range of interest. We find the lower and upper redshift limits of the volume-limit for the corresponding spectroscopic subsample s in order to calculate n_i^s .

Galaxy clustering has been measured at intermediate and small scales (Zehavi et al. 2005, 2010; Masjedi et al. 2006; Chen 2009; Li & White 2010; White et al. 2011). Our results are consistent with the results of Zehavi et al. (2010) (see Figure 20). In order to generate our mass-threshold samples which are nearly the same as their luminosity-threshold samples, we calculated M^* , the mean mass of the galaxies nearby their luminosity-threshold M_r as our mass-threshold, and we cut $M_s > M^*$ and $M_i > M^*$ to generate the corresponding mass-threshold samples. This turns our cross-correlation into an auto-correlation. In order to calculate n_i^s for the two subsamples with $M_r < -18.0$ and $M_r < -18.5$ in Figure 20, we use the peak real-space number densities instead of the average real-space number densities, because there are no obvious volume-limit in these two subsamples.

Similarly, we can measure ρ_i and $w_{si}(r_p)$ separately instead of $\rho_i w_{si}(r_p)$.

In order to show that our result successfully corrected the fiber collisions, we compare our result with the extension of the best-fit power law from Zehavi et al. (2010), see Figure 21 and 22. The extension dashed line is from the power fit of the first six data points of Zehavi et al. (2010) in the range $0.25 h_{70}^{-1} \text{ Mpc} \lesssim r_p \lesssim 2.5 h_{70}^{-1} \text{ Mpc}$. We cut at $r_p \approx 2.5 h_{70}^{-1} \text{ Mpc}$ because there is a sharp break at $r_p \approx 2.5 h_{70}^{-1} \text{ Mpc}$ which will be discussed at the end of Section 5. On the other side, this extension is very robust. In Figure 22, the difference is very small among the three extension dashed lines using the first five, first six and first seven data points of Zehavi et al. (2010). Our result (the triangle data points) with correction of fiber collisions fits better than the result assuming $p_j = 1$ and $f_j = 1$ (the diamond data points). We also show the data point before photometry correction Figure 22.

4.2. Comparison to previous merger rate results

Please note that the merger time error will be shown in the error bars in the figures from now on.

Our results are consistent with recent measurements of the merger rates based on counts of close pairs (Masjedi et al. 2008; Patton & Atfield 2008; Kitzbichler & White 2008; Bundy et al. 2009; De Propriis et al. 2010; Robaina et al. 2010). The low dry merger rate an upper limit of $1.8 h_{70}$ percent per Gyr for massive red galaxies (red9) under assumption of $t_{merge} = t_{BT,i}$ here is in good agreement with a number of other estimates: at

$z < 0.36$, Masjedi et al. (2008) obtained an upper limit of $1.2 h_{70}$ percent per Gyr (converted from $1.7 h$ percent per Gyr) for the dry merger rate of SDSS LRGs with $M_i < -22.75$; at $0.45 < z < 0.65$, De Propris et al. (2010) determined a 5σ upper limit to the dry merger rate of $0.7 h_{70}$ percent per Gyr (converted from $1.0 h$ percent per Gyr) for galaxies with $-23 < M(r)_{k+e,z=0.2} + 5 \log h < -21.5$ in the 2dF-SDSS LRG and QSO (2SLAQ) redshift survey.

Robaina et al. (2010) found that the fraction of galaxies ($M > 5 \times 10^{10} h_{70}^{-2} M_{\odot}$) in pairs separated between 15 and $30 h_{70}^{-1}$ kpc in 3D space is $f_{3Dpair}^{15-30 h_{70}^{-1} \text{ kpc}} = 0.01$ at $z = 0.1$, which is calculate by $(1.0 - 0.3) \times F(z)$, because they find that $30 \sim 40$ percent of galaxies in close pairs have $r < 15 h_{70}^{-1}$ kpc separations. They also expect most of the mergers to be majors; *i.e.*, with mass ratio between 1:1 and 1:4. Our result of $f_{3Dpair}^{15-30 h_{70}^{-1} \text{ kpc}}$ is 0.02 at $0.03 < z < 0.15$ with mass ratio between 1:1 and 1:4, which is consistent with the result of Robaina et al. (2010).

With $t_{merge} = t_{KW,i}$ determined, we compute the volumetric merger rate (the number of mergers per unit time per unit comoving volume) as a function of the stellar mass of the primary or host galaxy. We call this the *merger rate mass function* (merger rate MF) and denote it using the variable, Ψ . Figure 23 shows the comparison of our major merger rate MF at $0.03 < z < 0.15$ with the major merger rate MF of Bundy et al. (2009) at $0.4 < z < 0.7$ at mass ratio $m/M > 0.25$. We can see that both of Figures 23 and 24 show that our results are consistent with these previous results.

Our results are also consistent with recent merger rates predicted in theories of galaxy formation in a cosmological context (Maller et al. 2006; Stewart et al. 2009). We estimate our merger rate R_{mg} at a certain mass ratio m/M by integrating Γ_i in equation (29). We compare our R_{mg} with the results of Maller et al. (2006) at mass ratio $m/M > 0.5$ (Figure 25) and the results of Stewart et al. (2009) at mass ratio $m/M > 0.3$ and $m/M > 0.6$ (Figure 26). We can see that both of Figures 25 and 26 show that our results are consistent with these previous results.

Wetzel & Tinker (2012) found that from redshift $z = 2$ to now, it is around 27 percent of galaxies similar to our Milky Way that experienced a merger with mass ratio $m/M > 0.1$, and around 11 percent that experienced a merger with mass ratio $m/M > 0.33$. In our research, the galaxies in blue7 or blue8 subsample are similar to our Milky Way. If we take our results under assumption of $t_{merge} = t_{KW,i}$ at face value and make the strong assumption that the growth happens at a non-evolving rate, from redshift $z = 2$ to now (a period of $\approx 10 h_{70}^{-1}$ Gyr), we expect the galaxies in blue7 or blue8 subsample to merge by ~ 21 percent with mass ratio $m/M > 0.1$, and ~ 10 percent with mass ratio $m/M > 0.33$, which is close to the result of Wetzel & Tinker (2012).

5. Discussion

We find that under the assumption of $t_{merge} = t_{KW,i}$, the total fractional accretion rates onto red main galaxies are from $[1.3 \pm 0.7]$ to $[3.7 \pm 1.9]$ h_{70} percent per Gyr depending on stellar mass, and those onto blue main galaxies are from $[0.6 \pm 0.3]$ to $[1.1 \pm 0.6]$ h_{70} percent per Gyr. We find that at fixed stellar mass, the total fractional accretion rates onto red galaxies is greater than that onto blue galaxies. The total fractional accretion rate is a stronger function of primary mass for red galaxies than that for blue galaxies. We also find that more than 60 percent of the total fractional accretion rates are from major mergers with mass ratio between 1 : 1 and 1 : 3, and less than 15 percent of the total fractional growth rates are from minor mergers with mass ratio between 1 : 10 and 1 : 100.

The first limitation of the imaging sample arises from the lack of spectroscopic information on the galaxies from the imaging sample. However, for galaxies from imaging sample with stellar masses $M_i > 6 \times 10^9 h_{70}^{-2} M_{\odot}$, we estimate the real-space number densities n_i from equation (35). So we measured n_i , ρ_i and $w_{si}(r_p)$ separately. But at stellar masses $M_i < 6 \times 10^9 h_{70}^{-2} M_{\odot}$, it is impossible to precisely measure the real-space number densities n_i , so that we cannot disentangle the clustering power from the number density for these small-mass galaxies from the imaging sample, and we only measure the products $n_i w_{si}(r_p)$ and $\rho_i w_{si}(r_p)$ but not either n_i , ρ_i or $w_{si}(r_p)$ separately.

The second limitation is removing galaxies from imaging sample with apparent magnitudes $r > 21.5$ mag because of the limitation of lack of imaging information on the galaxies of SDSS (see Figure 5). This cut of apparent magnitudes $r > 21.5$ mag will affect the minor mergers with mass ratio between 1 : 30 and 1 : 100 for the small stellar mass galaxies from spectroscopic samples red1~4 and blue1~4 at redshift $z \gtrsim 0.10$, and the number densities of the galaxies in these spectroscopic samples decrease sharply at redshift $z \gtrsim 0.10$ (see Figures 3 and 4), which will sharply reduce the effect of this cut. This cut will cause less than 5% error because the contribution of the minor mergers with mass ratio between 1 : 30 and 1 : 100 is only $< 5\%$. This assumption is good to take, because it will cause far below 5% error. In order to not affect the minor mergers with mass ratio between 1 : 30 and 1 : 100 at all, we need our imaging sample to be ~ 1 mag fainter than what we use now.

We can see ‘valleys’ at the third to fifth data points ($37.6 < r_p < 94.4 h_{70}^{-1}$ kpc) of the two minor-merger curves ($10^{-1.5} < M_i/M_s < 10^{-1}$ and $10^{-2} < M_i/M_s < 10^{-1.5}$) in each plot of Figures 10 through 13, which seems like a kind of issue due to photometric biases or bad deblending. However we do not think so, because the photometric biases and bad deblending are very small at separations large than 15 arcsec (see Table 1) and at ‘valleys’ (the third to fifth data points $37.6 < r_p < 94.4 h_{70}^{-1}$ kpc), the photometry correction is nearly zero (below 5%). Also, we do not think that the ‘valleys’ will make our conclusions invalid

even if that is an issue in minor merger, because from the above paragraph we know that only less than 15 percent of the total fractional accretion rates are from minor mergers with mass ratio between 1 : 10 and 1 : 100.

If we assume that the growth happens at a non-evolving rate from redshift $z = 1$ to now (a period of $\approx 8 h_{70}^{-1}$ Gyr), we expect the red galaxies to grow by about $[10 \pm 5]$ percent to $[28 \pm 14]$ percent depending on stellar mass under assumption of $t_{merge} = t_{KW,i}$, and the red L^* galaxies (around red7 and red8) grow by about $[20 \pm 10]$ percent. The merger rate may have been different in the past, of course, higher or lower (Lin et al. 2008; Chou et al. 2011). If we assume that the growth of massive red galaxies (L^* galaxies and above) is mainly from galaxy mergers, and also assume that the evolution of the galaxy merger rate per galaxy is proportional to $(1 + z)^{+3.0 \pm 1.1}$ (Lotz et al. 2011) from redshift $z = 1$ to now, we expect that the stellar mass density of the red massive galaxies (L^* galaxies and above) increased about ~ 75 percent under the assumption of $t_{merge} = t_{KW,i}$, or about ~ 40 percent under the assumption of $t_{merge} = t_{BT,i}$ (see Table 3), which are consistent with recent studies on the high-redshift Universe which find that the red sequence appears to grow in stellar mass over time by a factor of 50 percent to 100 percent from redshift $z = 1$ to now (Bell et al. 2004; Willmer et al. 2006; Blanton 2006; Faber et al. 2007; Conselice et al. 2007; Cimatti et al. 2008; van Dokkum et al. 2008; Saracco et al. 2009).

According to Section 4, our results are consistent with the previous clustering results of Zehavi et al. (2010). Our estimated merger rates are consistent with the merger rates estimated by counting of close pairs (Masjedi et al. 2008; Patton & Atfield 2008; Kitzbichler & White 2008; Bundy et al. 2009; De Propris et al. 2010; Robaina et al. 2010). Our estimated merger rates are also consistent with the merger rates predicted in theories of galaxy formation in a cosmological context (Maller et al. 2006; Stewart et al. 2009; Wetzel & Tinker 2012).

However, we found that not all merger studies find such low values when we compared our results with the studies at higher redshift. The morphological derivations of the merger fraction (*e.g.*, De Propris et al. 2007; Conselice et al. 2007; Lotz et al. 2006, 2008; Conselice et al. 2009) tend to find values of $f_{pair} \approx 0.1$ at $0.4 < z < 1.4$, about 2 times higher than the results of our pair analysis (see Figure 24). The discrepancy can be resolved easily if either (1) morphological signatures of merging last for many dynamical times (*e.g.*, tidal tails) or (2) the very minor mergers ($m/M < 0.25$) inflate the merger rates (please note that our pair analysis in Figure 24 are only estimated from major mergers at mass ratio $m/M > 0.25$) or (3) morphological tools for finding mergers maybe find some systems which are not involved in mergers or (4) merger rates per galaxy at high redshift may be larger than those at low redshift.

The total fractional accretion rates shown in the solid lines in Figure 19 are upper limits

on the true fractional mass growth. There are two reasons: (1) we assume $t_{merge,i} = t_{KW,i}$ for every pair. However it is not true for close pairs in high velocity dispersion, (2) we assume that the stellar mass growth of the central galaxies from the spectroscopic sample is equal to the stellar mass of the galaxy from the imaging sample, see equation (30). However Lin et al. (2004) found that up to 50 percent of the stars in the galaxies from the imaging sample could be stripped off before the merger with LRGs is complete. So our mass growth rate under the assumption of $t_{merge} = t_{KW,i}$ is an upper limit on the growth by merging.

We find that the accretion onto red and massive blue galaxies is dominated by mergers with red companions, and that onto small-mass blue galaxies, red and blue companions make comparable contributions, this is shown by Table 2 and Figures 17 and 18. So, most of the mass brought into red galaxies by merging is brought by “dry mergers” (Bell et al. 2006b; van Dokkum 2005; Masjedi et al. 2008).

We find that all the contributions to growth decrease with decreasing stellar mass at the small-mass end for all of 18 spectroscopic subsamples. The contribution to growth decreases with decreasing M_i/M_s since $M_i/M_s < 0.4$. For all 18 subsamples, the curves essentially decrease to zero by $M_i/M_s < 0.01$ for $t_{merge} = t_{KW,i}$ and by $M_i/M_s < 0.1$ for $t_{merge} = t_{BT,i}$, so calculation of the total amount of mass brought in by merger activities does not require consideration of galaxies from the imaging sample with $M_i/M_s < 0.01$.

From Figures 10 through 13 and Figure 20, we find a sharp break at $r_p \approx 2.5 h_{70}^{-1}$ Mpc and a less-sharp transition at $r_p \approx 0.43 h_{70}^{-1}$ Mpc. These two transitions are also found in LRGs by Masjedi et al. (2008), which can be explained in the context of the “halo occupation” picture of galaxy clustering (Peacock & Smith 2000; Scoccimarro et al. 2001; Berlind & Weinberg 2002; Cooray & Sheth 2002; Zheng et al. 2005; Watson et al. 2010, 2012): (1) the mergers at $r_p < 0.43 h_{70}^{-1}$ Mpc are the one-halo mergers (both of the two merging galaxies are inside one halo); (2) the mergers at $r_p > 2.5 h_{70}^{-1}$ Mpc are the two-halo mergers (the two merging galaxies are separately inside two nearby halos); (3) the mergers at $0.43 < r_p < 2.5 h_{70}^{-1}$ Mpc are the mixed-halo mergers (some of the mergers are the one-halo mergers, the others are the two-halo mergers). So at $r_p \approx 0.43 h_{70}^{-1}$ Mpc the mergers transfer from the one-halo mergers to the mixed-halo mergers, and at $r_p \approx 2.5 h_{70}^{-1}$ Mpc the mergers transfer from the mixed-halo mergers to the two-halo mergers. These two transitions are clearer in Figure 10 of mergers between two red galaxies than that in the other three figures.

It is a pleasure to thank Douglas Watson, Jeremy Tinker and our anonymous referee for valuable input.

This research made use of public SDSS data. Funding for the SDSS and SDSS-II has been provided by the Alfred P. Sloan Foundation, the Participating Institutions, the National

Science Foundation, the U.S. Department of Energy, the National Aeronautics and Space Administration, the Japanese Monbukagakusho, the Max Planck Society, and the Higher Education Funding Council for England. The SDSS Web Site is <http://www.sdss.org/>.

SDSS is managed by the Astrophysical Research Consortium for the Participating Institutions. The Participating Institutions are the American Museum of Natural History, Astrophysical Institute Potsdam, University of Basel, University of Cambridge, Case Western Reserve University, University of Chicago, Drexel University, Fermilab, the Institute for Advanced Study, the Japan Participation Group, Johns Hopkins University, the Joint Institute for Nuclear Astrophysics, the Kavli Institute for Particle Astrophysics and Cosmology, the Korean Scientist Group, the Chinese Academy of Sciences (LAMOST), Los Alamos National Laboratory, the Max-Planck-Institute for Astronomy (MPIA), the Max-Planck-Institute for Astrophysics (MPA), New Mexico State University, Ohio State University, University of Pittsburgh, University of Portsmouth, Princeton University, the United States Naval Observatory, and the University of Washington.

REFERENCES

- Abazajian, K. et al. 2003, *AJ*, 126, 2081
- Abazajian, K. et al. 2004, *AJ*, 128, 502
- Abraham, R. G., Tanvir, N. R., Santiago, B. X., Ellis, R. S., Glazebrook, K., & van den Bergh, S. 1996, *MNRAS*, 279, L47
- Barnes, J. E., & Hernquist, L. 1996, *ApJ*, 471, 115
- Bell, E. F., Wolf, C., Meisenheimer, K., Rix, H.-W., Borch, A., Dye, S., Kleinheinrich, M., Wisotzki, L., & McIntosh, D. H. 2004, *ApJ*, 608, 752
- Bell, E. F. et al. 2005, *ArXiv Astrophysics e-prints*
- Bell, E. F., Phleps, S., Somerville, R. S., Wolf, C., Borch, A., & Meisenheimer, K. 2006, *ApJ*, 652, 270
- Bell, E. F., et al. 2006, *ApJ*, 640, 241
- Berlind, A. A. & Weinberg, D. H. 2002, *ApJ*, 575, 587
- Binney, J., & Tremaine, S. 1987, Princeton, NJ, Princeton University Press, 1987, 747 p.,
- Blanton, M. R. et al. 2003b, *ApJ*, 594, 186
- Blanton, M. R., et al. 2005, *AJ*, 129, 2562
- Blanton, M. R. 2006, *ApJ*, 648, 268
- Blanton, M. R., & Roweis, S. 2007, *AJ*, 133, 734
- Blanton, M. R., & Moustakas, J. 2009, *ARA&A*, 47, 159
- Boylan-Kolchin, M., & Ma, C.-P. 2007, *MNRAS*, 374, 1227
- Brown, M. J. I., Dey, A., Jannuzi, B. T., Brand, K., Benson, A. J., Brodwin, M., Croton, D. J., & Eisenhardt, P. R. 2007, *ApJ*, 654, 858
- Bundy, K., et al. 2006, *ApJ*, 651, 120
- Bundy, K., Fukugita, M., Ellis, R. S., Targett, T. A., Belli, S., & Kodama, T. 2009, *ApJ*, 697, 1369
- Carlberg, R. G., Pritchet, C. J., & Infante, L. 1994, *ApJ*, 435, 540

- Carlberg, R. G., et al. 2000, *ApJ*, 532, L1
- Carlberg, R. G., Yee, H. K. C., Morris, S. L., Lin, H., Hall, P. B., Patton, D., Sawicki, M., & Shepherd, C. W. 2000, *ApJ*, 542, 57
- Chen, J. 2009, *A&A*, 494, 867
- Chou, R. C. Y., Bridge, C. R., & Abraham, R. G. 2011, *AJ*, 141, 87
- Cimatti, A., Daddi, E., & Renzini, A. 2006, *A&A*, 453, L29
- Cimatti, A., et al. 2008, *A&A*, 482, 21
- Conroy, C., Ho, S., & White, M. 2007, *MNRAS*, 379, 1491
- Conselice, C. J., Bershad, M. A., Dickinson, M., & Papovich, C. 2003, *AJ*, 126, 1183
- Conselice, C. J. et al. 2007, *MNRAS*, 381, 962
- Conselice, C. J., Yang, C., & Bluck, A. F. L. 2009, *MNRAS*, 394, 1956
- Cool, R. J., et al. 2008, *ApJ*, 682, 919
- Cooray, A., & Sheth, R. 2002, *Phys. Rep.*, 372, 1
- Courteau, S., Dutton, A. A., van den Bosch, F. C., MacArthur, L. A., Dekel, A., McIntosh, D. H., & Dale, D. A. 2007, *ApJ*, 671, 203
- Daddi, E., et al. 2005, *ApJ*, 626, 680
- Davis, M. & Peebles, P. J. E. 1983, *ApJ*, 267, 465
- De Propris, R., Conselice, C. J., Liske, J., Driver, S. P., Patton, D. R., Graham, A. W., & Allen, P. D. 2007, *ApJ*, 666, 212
- de Ravel, L., Le Fèvre, O., Tresse, L., et al. 2009, *A&A*, 498, 379
- De Propris, R., et al. 2010, *AJ*, 139, 794
- Faber, S. M. et al. 2007, *ApJ*, 665, 265
- Fukugita, M., Ichikawa, T., Gunn, J. E., Doi, M., Shimasaku, K., & Schneider, D. P. 1996, *AJ*, 111, 1748
- Gunn, J. E., Carr, M. A., Rockosi, C. M., Sekiguchi, M., et al. 1998, *AJ*, 116, 3040

- Gunn, J. E., et al. 2006, *AJ*, 131, 2332
- Hogg, D. W. 1999, arXiv:astro-ph/9905116
- Hogg, D. W., et al. 2004, *ApJ*, 601, L29
- Kartaltepe, J. S., et al. 2007, *ApJS*, 172, 320
- Kitzbichler, M. G., & White, S. D. M. 2008, *MNRAS*, 391, 1489
- Li, C., & White, S. D. M. 2010, *MNRAS*, 407, 515
- Lin, L., et al. 2004, *ApJ*, 617, L9
- Lin, L., Patton, D. R., Koo, D. C., et al. 2008, *ApJ*, 681, 232
- Longhetti, M., et al. 2007, *MNRAS*, 374, 614
- Lotz, J. M., Madau, P., Giavalisco, M., Primack, J., & Ferguson, H. C. 2006, *ApJ*, 636, 592
- Lotz, J. M., et al. 2008, *ApJ*, 672, 177
- Lotz, J. M., Jonsson, P., Cox, T. J., & Primack, J. R. 2010, *MNRAS*, 404, 590
- Lotz, J. M., Jonsson, P., Cox, T. J., et al. 2011, *ApJ*, 742, 103
- Masjedi, M., et al. 2006, *ApJ*, 644, 54
- Masjedi, M., Hogg, D. W., & Blanton, M. R. 2008, *ApJ*, 679, 260
- Maller, A. H., Katz, N., Kereš, D., Davé, R., & Weinberg, D. H. 2006, *ApJ*, 647, 763
- Murali, C., Katz, N., Hernquist, L., Weinberg, D. H., & Davé, R. 2002, *ApJ*, 571, 1
- Naab, T., & Burkert, A. 2003, *ApJ*, 597, 893
- Patton, D. R., Pritchett, C. J., Yee, H. K. C., Ellingson, E., & Carlberg, R. G. 1997, *ApJ*, 475, 29
- Patton, D. R., Carlberg, R. G., Marzke, R. O., Pritchett, C. J., da Costa, L. N., & Pellegrini, P. S. 2000, *ApJ*, 536, 153
- Patton, D. R., & Atfield, J. E. 2008, *ApJ*, 685, 235
- Patton, D. R., Ellison, S. L., Simard, L., McConnachie, A. W., & Mendel, J. T. 2011, *MNRAS*, 412, 591

- Peacock, J. A. & Smith, R. E. 2000, MNRAS, 318, 1144
- Quintero, A. D., et al. 2004, ApJ, 602, 190
- Robaina, A. R., Bell, E. F., van der Wel, A., Somerville, R. S., Skelton, R. E., McIntosh, D. H., Meisenheimer, K., & Wolf, C. 2010, ApJ, 719, 844
- Scarlata, C., et al. 2007, ApJS, 172, 494
- Scoccimarro, R., Sheth, R. K., Hui, L., & Jain, B. 2001, ApJ, 546, 20
- Stewart, K. R., Bullock, J. S., Barton, E. J., & Wechsler, R. H. 2009, ApJ, 702, 1005
- Stoughton, C. et al. 2002, AJ, 123, 485
- Strauss, M. A., et al. 2002, AJ, 124, 1810
- Strateva, I., et al. 2001, AJ, 122, 1861
- Saracco, P., Longhetti, M., & Andreon, S. 2009, MNRAS, 392, 718
- Trujillo, I., Conselice, C. J., Bundy, K., Cooper, M. C., Eisenhardt, P., & Ellis, R. S. 2007, MNRAS, 382, 109
- Toft, S., et al. 2007, ApJ, 671, 285
- van Dokkum, P. G., Franx, M., Fabricant, D., Kelson, D. D., & Illingworth, G. D. 1999, ApJ, 520, L95
- van Dokkum, P. G. 2005, AJ, 130, 2647
- van Dokkum, P. G., et al. 2008, ApJ, 677, L5
- Wake, D. A. et al. 2006, MNRAS, 372, 537
- Watson, D. F., Berlind, A. A., McBride, C. K., & Masjedi, M. 2010, ApJ, 709, 115
- Watson, D. F., Berlind, A. A., McBride, C. K., Hogg, D. W., & Jiang, T. 2012, ApJ, 749, 83
- White, M., et al. 2011, ApJ, 728, 126
- Wetzel, A., & Tinker, J. 2012, in preparation
- Willmer, C. N. A., et al. 2006, ApJ, 647, 853

York, D., et al. 1999, *Bulletin of the American Astronomical Society*, 31, 1452

York, D. G., & SDSS Collaboration 2001, *Bulletin of the American Astronomical Society*, 33, 906

Zehavi, I., et al. 2005, *ApJ*, 621, 22

The SDSS Collaboration: Zehavi et al. 2010, arXiv:1005.2413

Zepf, S. E. & Koo, D. C. 1989, *ApJ*, 337, 34

Zheng, Z., et al. 2005, *ApJ*, 633, 791

Zhu, G., Blanton, M. R., & Moustakas, J. 2010, *ApJ*, 722, 491

Zhu, G., et al. 2011, *ApJ*, 726, 110

Table 1. Spectroscopic Subsamples

Subsample	$\langle M \rangle^a$ [$10^{10} h_{70}^{-2} M_{\odot}$]	number	$\langle z \rangle^b$	z_{min}^c	z_{max}^d	σ_v or V_c^e [km s^{-1}]	angular separation ^f [arcsec]
red0							
red1	1.00	11115	0.052	0.05	0.055	88.8	35.0 and 55.4
red2	1.61	17023	0.064	0.05	0.077	105	28.5 and 45.1
red3	2.26	20585	0.073	0.05	0.088	119	25.2 and 39.9
red4	2.99	22904	0.081	0.05	0.103	131	22.7 and 36.0
red5	3.81	25184	0.090	0.05	0.115	143	20.6 and 32.6
red6	4.77	27809	0.099	0.05	0.127	155	18.8 and 29.8
red7	5.95	31390	0.108	0.05	0.137	167	17.1 and 27.2
red8	7.72	34919	0.113	0.05	0.150	183	16.4 and 26.0
red9	13.5	40036	0.116	0.05	0.150	223	16.0 and 25.4
blue0							
blue1	0.96	36470	0.069	0.05	0.070	123	26.6 and 42.2
blue2	1.59	30562	0.080	0.05	0.086	137	22.9 and 36.3
blue3	2.25	26992	0.090	0.05	0.105	148	20.5 and 32.6
blue4	2.98	24688	0.099	0.05	0.116	157	18.8 and 29.8
blue5	3.80	22404	0.106	0.05	0.129	166	17.5 and 27.7
blue6	4.75	19774	0.112	0.05	0.140	175	16.6 and 26.3
blue7	5.92	16197	0.115	0.05	0.150	184	16.1 and 25.5
blue8	7.65	12667	0.117	0.05	0.150	197	16.0 and 25.3
blue9	11.6	7551	0.120	0.05	0.150	219	15.6 and 24.6

Note. — Information for the galaxies in the spectroscopic subsamples.

^a Mean stellar mass of galaxies in the corresponding spectroscopic subsample.

^b Mean redshift of galaxies in the corresponding spectroscopic subsample.

^c Lower redshift limit used.

^d Upper redshift limit used.

^e We show adopted velocity dispersion σ_v for the red galaxies and adopted circular velocity

V_c for the blue galaxies.

^f We show the angular separations of $r_p = 37.6h_{70}^{-1}$ kpc and $r_p = 59.6h_{70}^{-1}$ kpc which are the separations of the third and fourth data points in Figures 10 through 13.

Table 2. Fractional mass growth measurements

Subsample	$d(\ln M) / dt _{BT}{}^a$ [$10^{-3} h_{70} \text{ Gyr}^{-1}$]	blue fraction b [%]	$d(\ln M) / dt _{KW}{}^c$ [$10^{-3} h_{70} \text{ Gyr}^{-1}$]	blue fraction d [%]
red0				
red1	7.9 ± 4.2 e	27.3	13.0 ± 6.8	31.5
red2	9.1 ± 4.8	28.3	14.6 ± 7.6	31.4
red3	10.2 ± 5.3	25.3	16.3 ± 8.5	29.3
red4	11.8 ± 6.1	21.9	18.9 ± 9.7	26.3
red5	12.5 ± 6.4	23.6	20.3 ± 10.4	27.7
red6	13.0 ± 6.7	20.9	21.2 ± 10.9	25.6
red7	14.3 ± 7.3	20.7	23.6 ± 12.1	25.3
red8	15.2 ± 7.8	19.1	26.1 ± 13.3	23.5
red9	18.2 ± 9.3	11.8	37.4 ± 19.0	15.7
blue0				
blue1	3.2 ± 1.7	48.3	6.0 ± 3.1	46.5
blue2	3.6 ± 1.9	47.3	6.6 ± 3.4	47.0
blue3	3.8 ± 1.9	44.1	6.8 ± 3.5	45.1
blue4	3.9 ± 2.0	40.7	6.9 ± 3.5	43.2
blue5	4.3 ± 2.2	42.4	7.2 ± 3.8	45.8
blue6	4.6 ± 2.4	36.0	7.7 ± 4.0	41.6
blue7	4.8 ± 2.6	36.8	8.3 ± 4.4	42.2
blue8	5.5 ± 2.9	27.9	9.5 ± 5.0	34.4
blue9	5.3 ± 2.9	23.0	10.5 ± 5.7	28.4

Note. — Fractional mass growth of Main Galaxy by merging $h_{70} \text{ Gyr}^{-1}$, split by spectroscopic subsample.

^a Measurements under the assumption $t_{merge,i} = t_{BT,i}$.

^b Percent contribution of the blue galaxies from the imaging sample under the assumption $t_{merge,i} = t_{BT,i}$.

^c Measurements under the assumption $t_{merge,i} = t_{KW,i}$.

^d Percent contribution of the blue galaxies from the imaging sample under the assumption

$$t_{merge,i} = t_{KW,i}.$$

^e Errors are estimated including the error from merger time.

Table 3. Fractional mass growth measurements for massive red galaxies

Subsample	$d(\ln M) / dt _{BT}^a$ [$10^{-3} h_{70} \text{ Gyr}^{-1}$]	$d(\ln M) / dt _{KW}^b$ [$10^{-3} h_{70} \text{ Gyr}^{-1}$]
red7	31.8 ± 15.9^c	52.6 ± 26.3
red8	33.8 ± 16.9	58.1 ± 29.1
red9	40.5 ± 20.3	83.1 ± 41.6
$\gtrsim L^*$ red7~9	37.0 ± 18.5	70.5 ± 35.3
$\geq L^*$ red8~9	38.3 ± 19.1	74.9 ± 37.4
LRG red9	40.5 ± 20.3	83.1 ± 41.6

Note. — Fractional mass growth measurements for massive red galaxies (L^* galaxies and above) under assumption of merger rates $\propto (1+z)^{+3.0\pm 1.1}$, split by spectroscopic subsample.

^a Measurements under the assumption $t_{merge,i} = t_{BT,i}$.

^b Measurements under the assumption $t_{merge,i} = t_{KW,i}$.

^c Errors are estimated including the error from merger time.

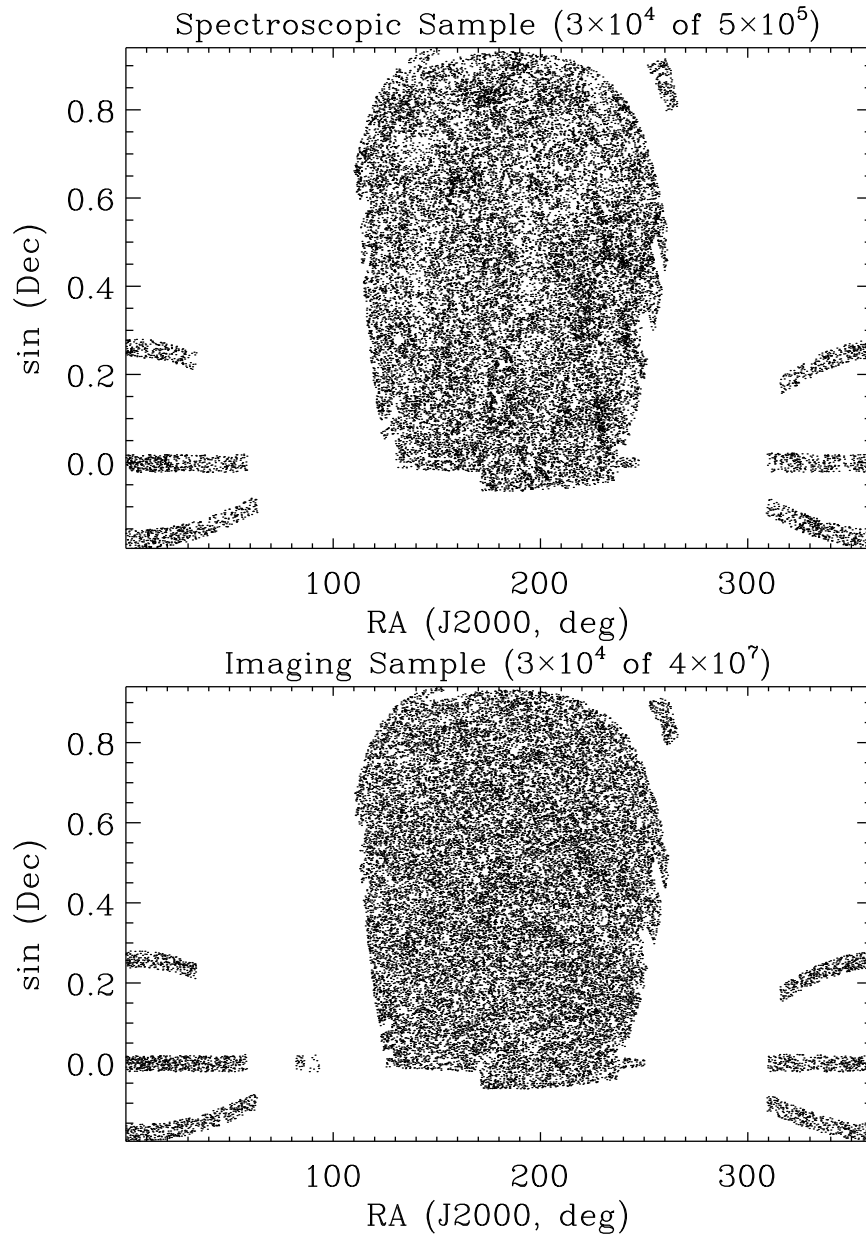


Fig. 1.— Sky distribution of the spectroscopic and imaging samples. For clarity, only a randomly chosen subsample of 3×10^4 points is shown in each case.

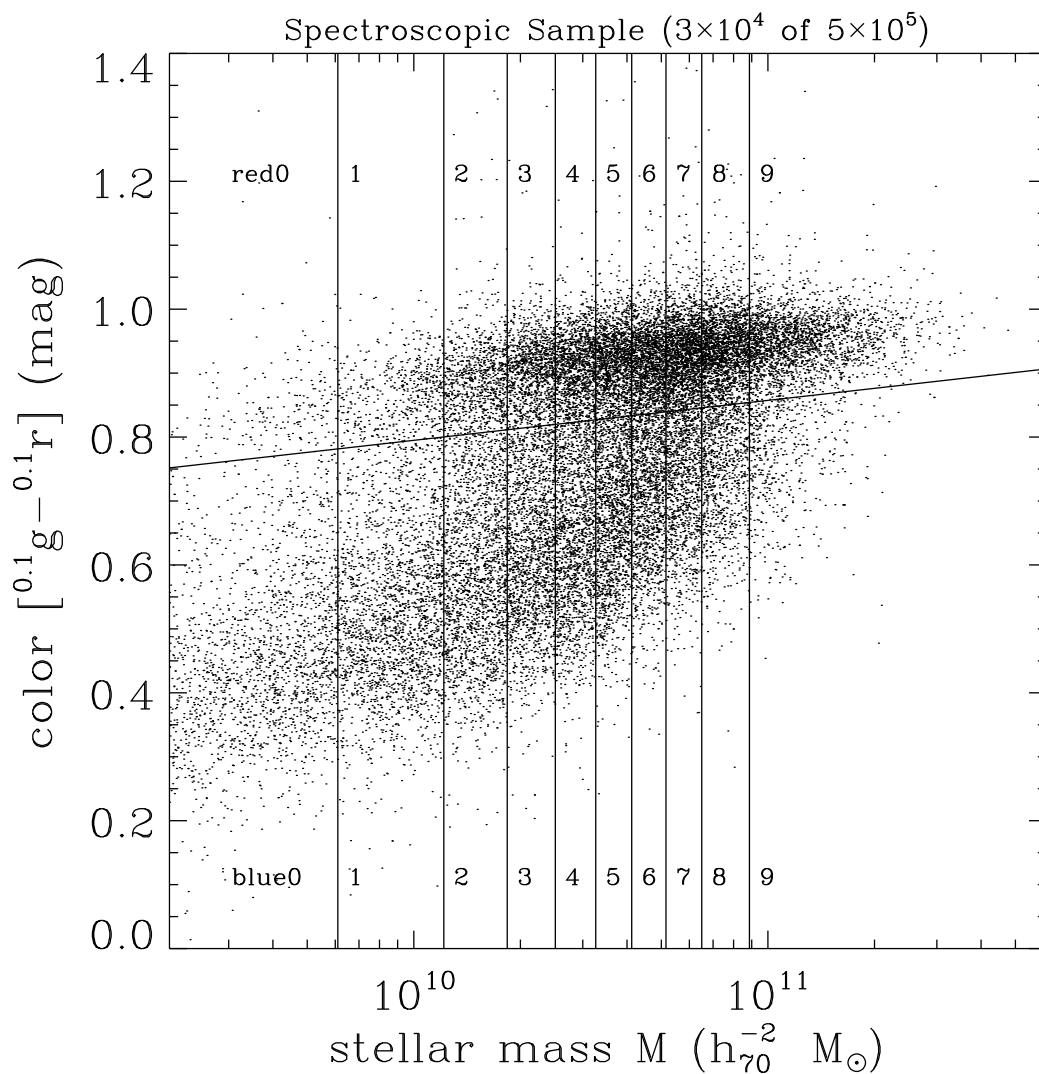


Fig. 2.— Distribution of the spectroscopic subsample in color and K -correct-estimated stellar mass. The nearly horizontal line separates galaxies into red and blue; the vertical lines separate galaxies into 10 subsamples with different stellar mass. For clarity, only a randomly chosen subsample of 3×10^4 points is shown.

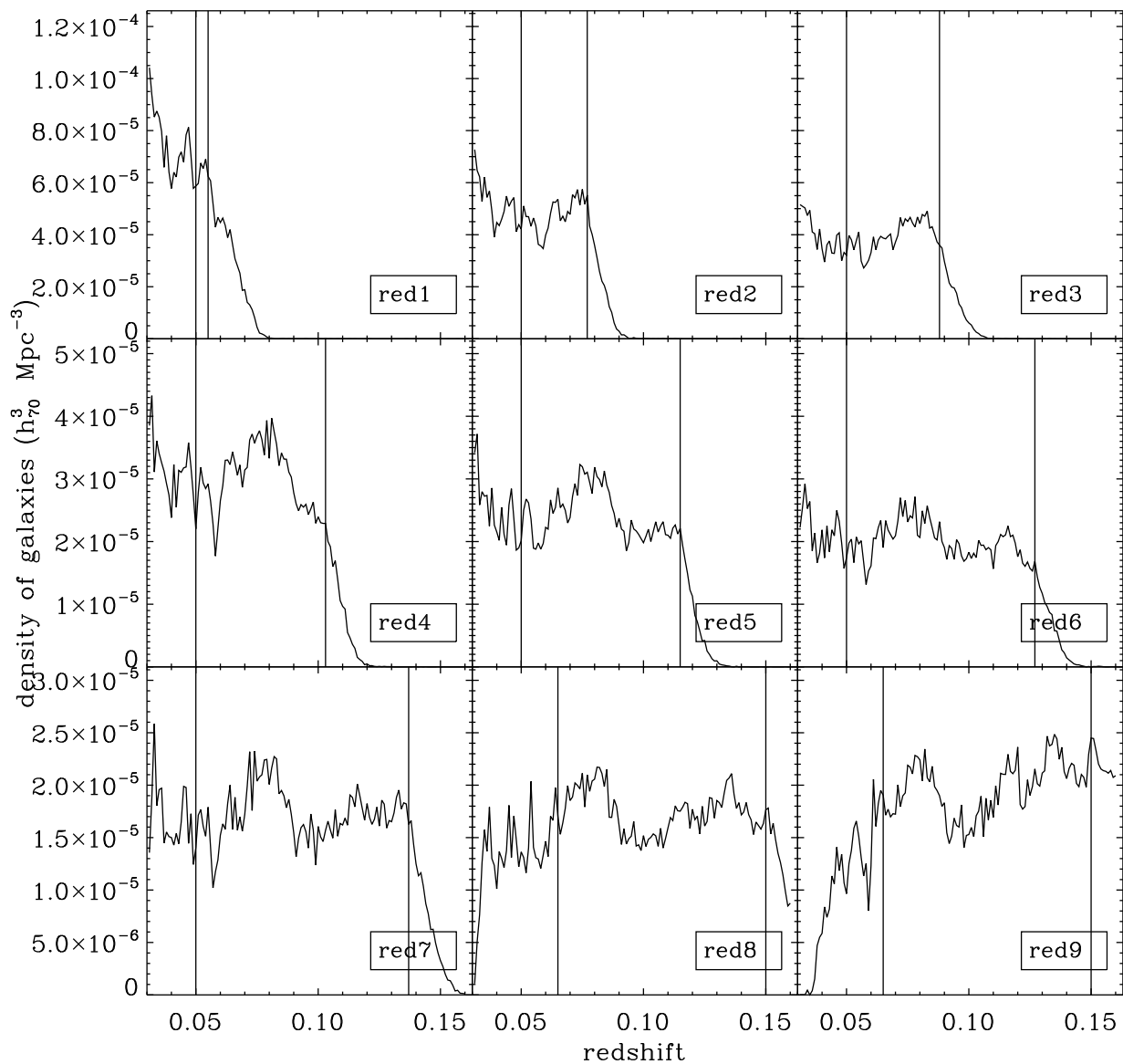


Fig. 3.— The number densities of each of the 9 red spectroscopic subsamples as a function of redshift. The vertical lines in each graph show the redshift limits used. The number density in red9 appears to rise with redshift, because we have removed galaxies with $r < 14$ mag (see text).

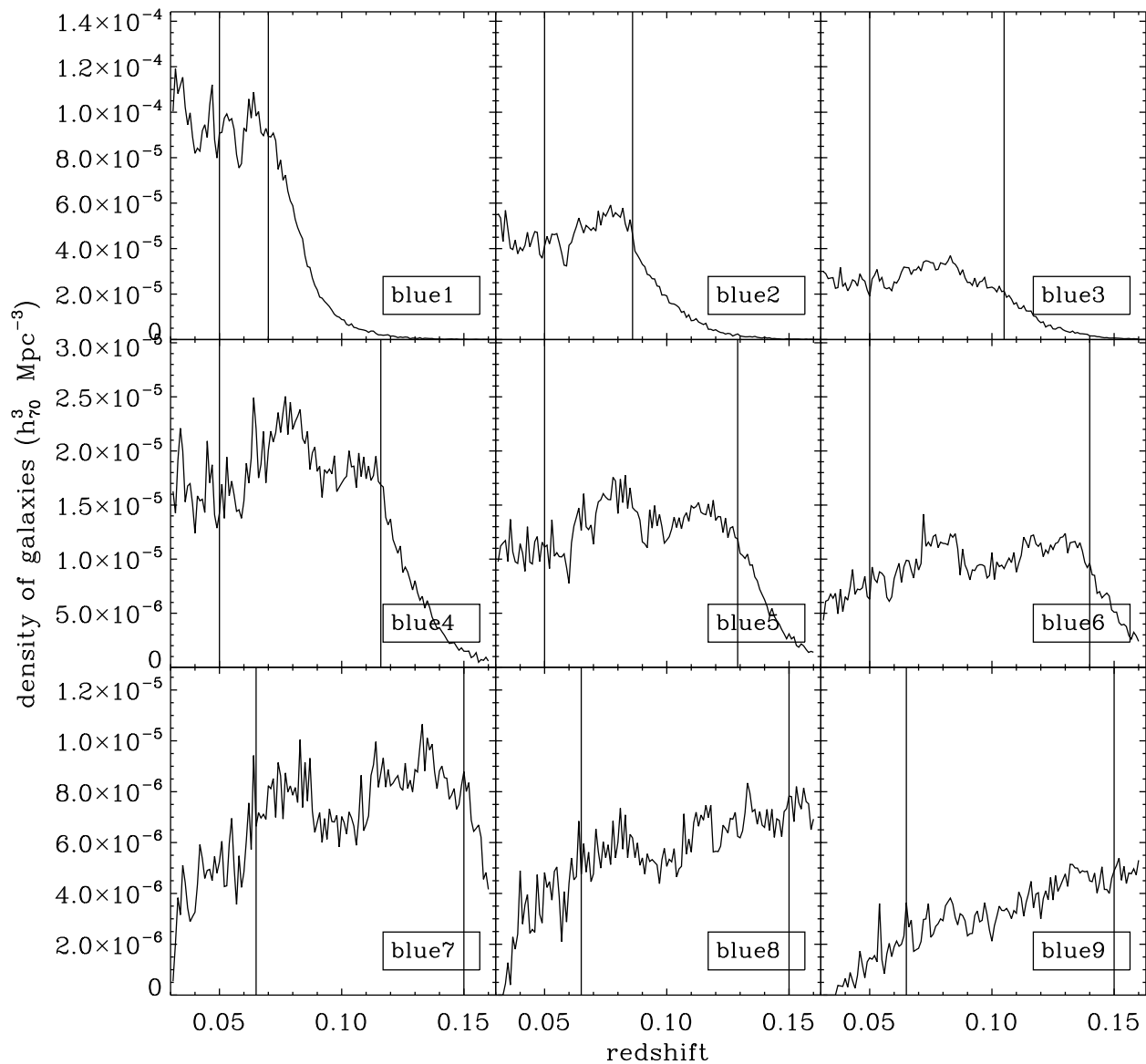


Fig. 4.— Same as Figure 3, but for the 9 blue spectroscopic subsamples. The number density in blue8 and blue9 appears to rise with redshift, because we have removed galaxies with $r < 14$ mag (see text).

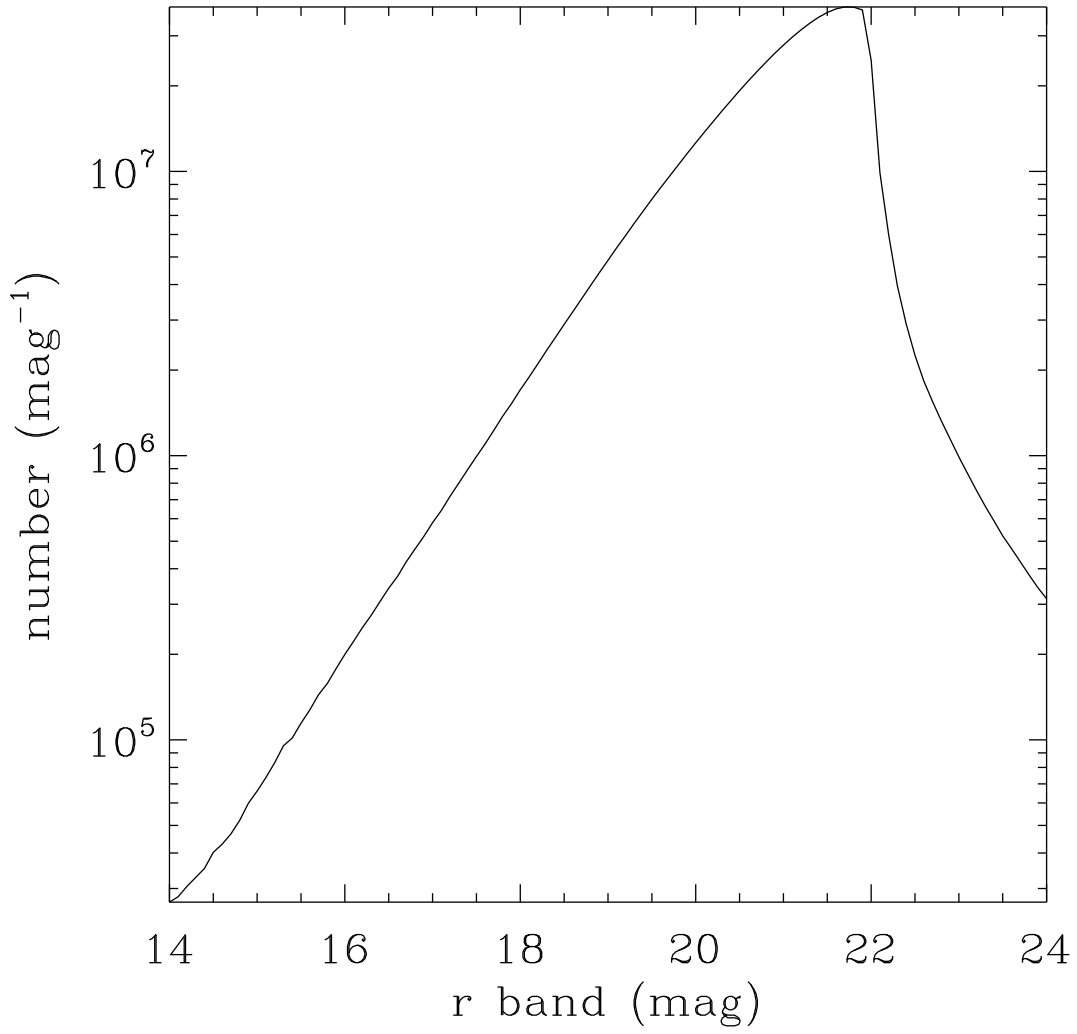


Fig. 5.— Distribution of apparent r magnitude for the imaging sample. We use only galaxies from the imaging sample with $14 < r < 21.5$ mag.

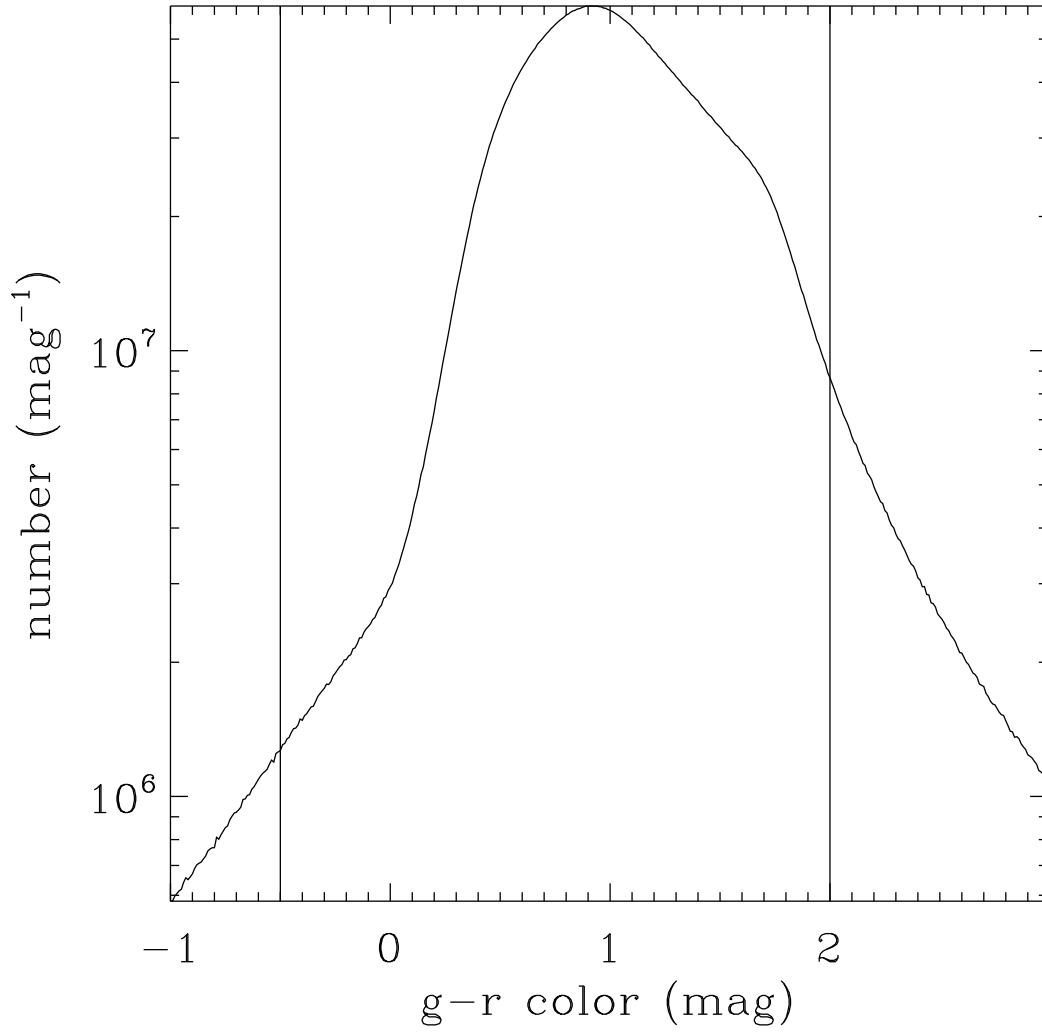


Fig. 6.— Distribution of $[g-r]$ color for the imaging sample. We use only galaxies from the imaging sample with $-0.5 < [g-r] < 2.0$ mag.

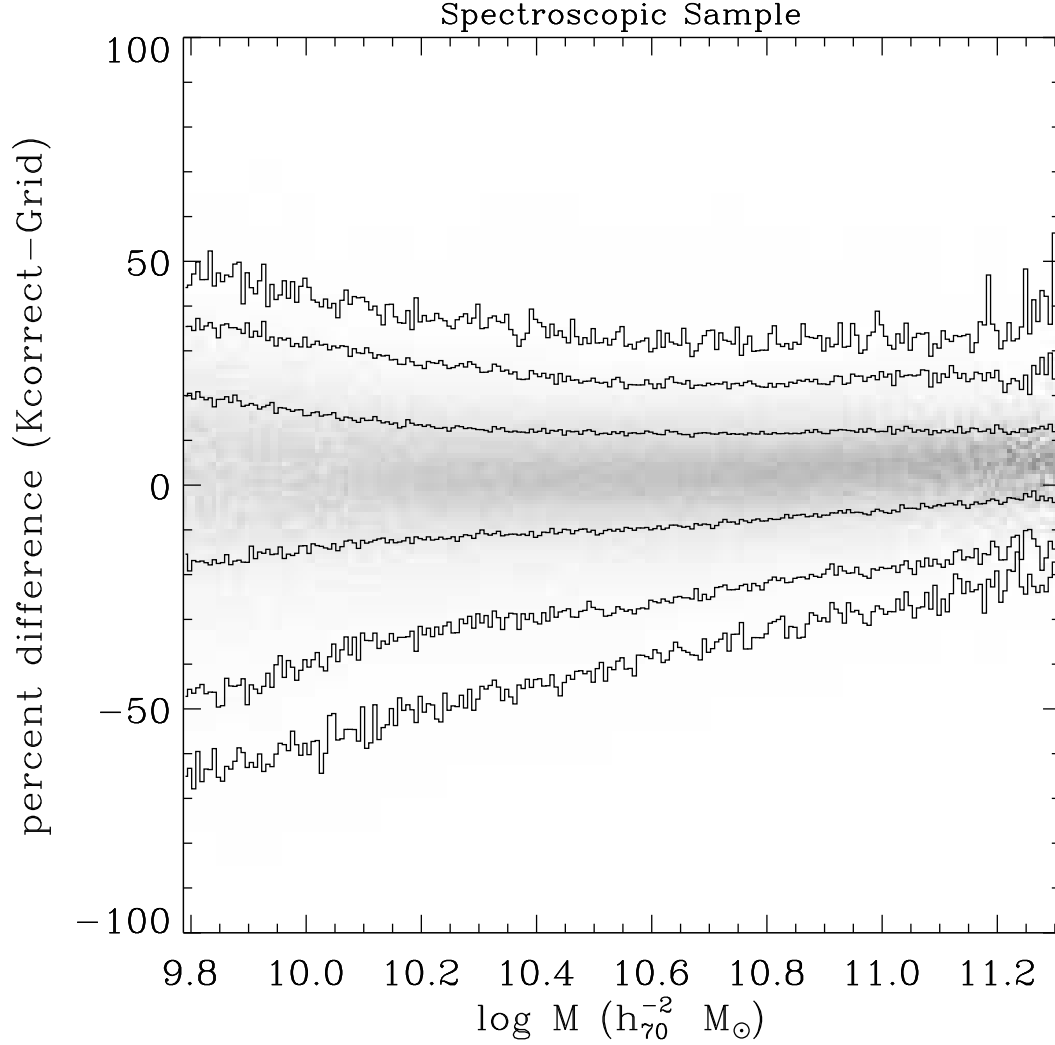


Fig. 7.— The difference between the K -correct-estimated stellar mass and the stellar mass estimated by the Grid Method. The contours show the 68, 95 and 99-percent intervals. The greyscale reflects the number of galaxies in each bin.

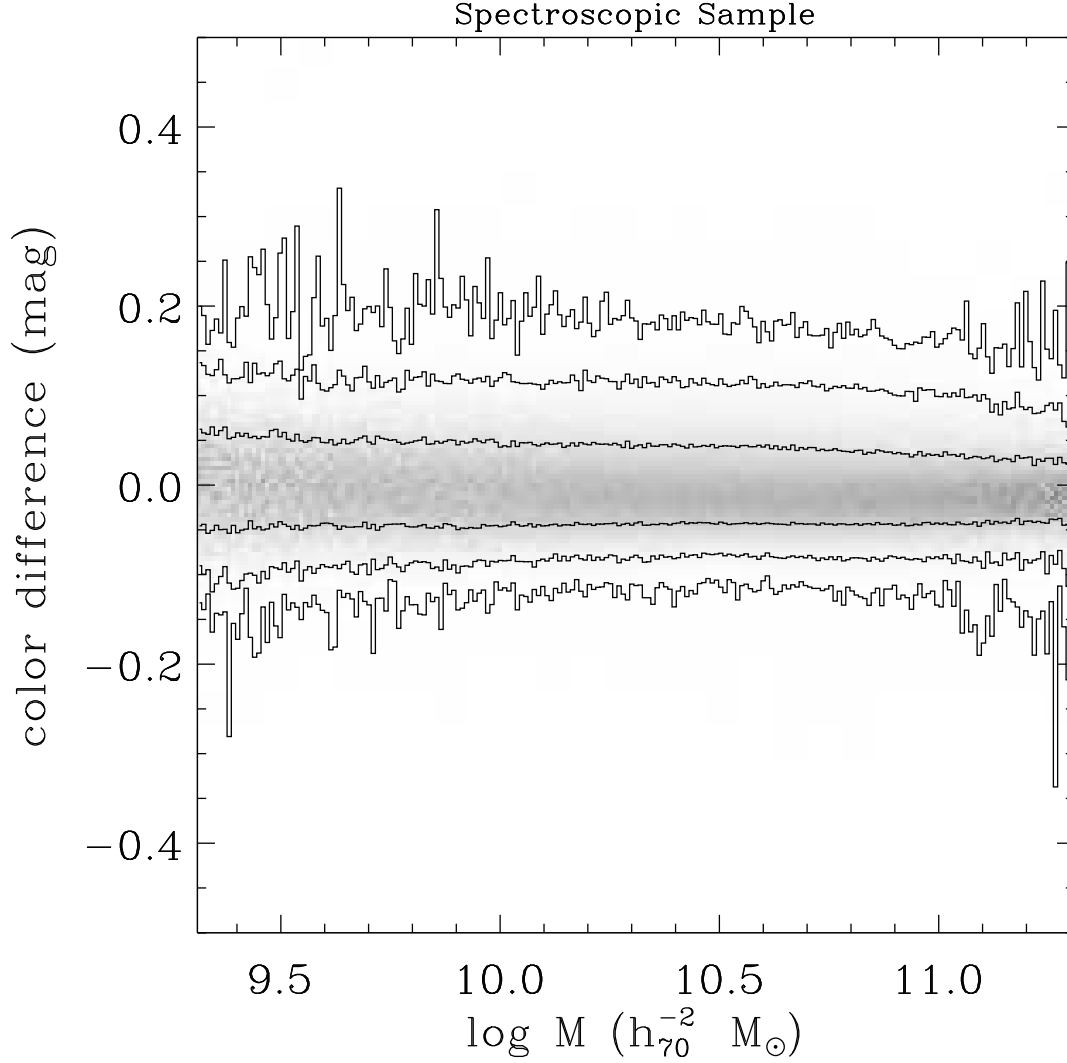


Fig. 8.— The difference between the K -correct-estimated $[^{0.1}g - ^{0.1}r]$ color and the $[^{0.1}g - ^{0.1}r]$ color estimated by the Grid Method. The greyscale and the contours are similar to those in Figure 7.

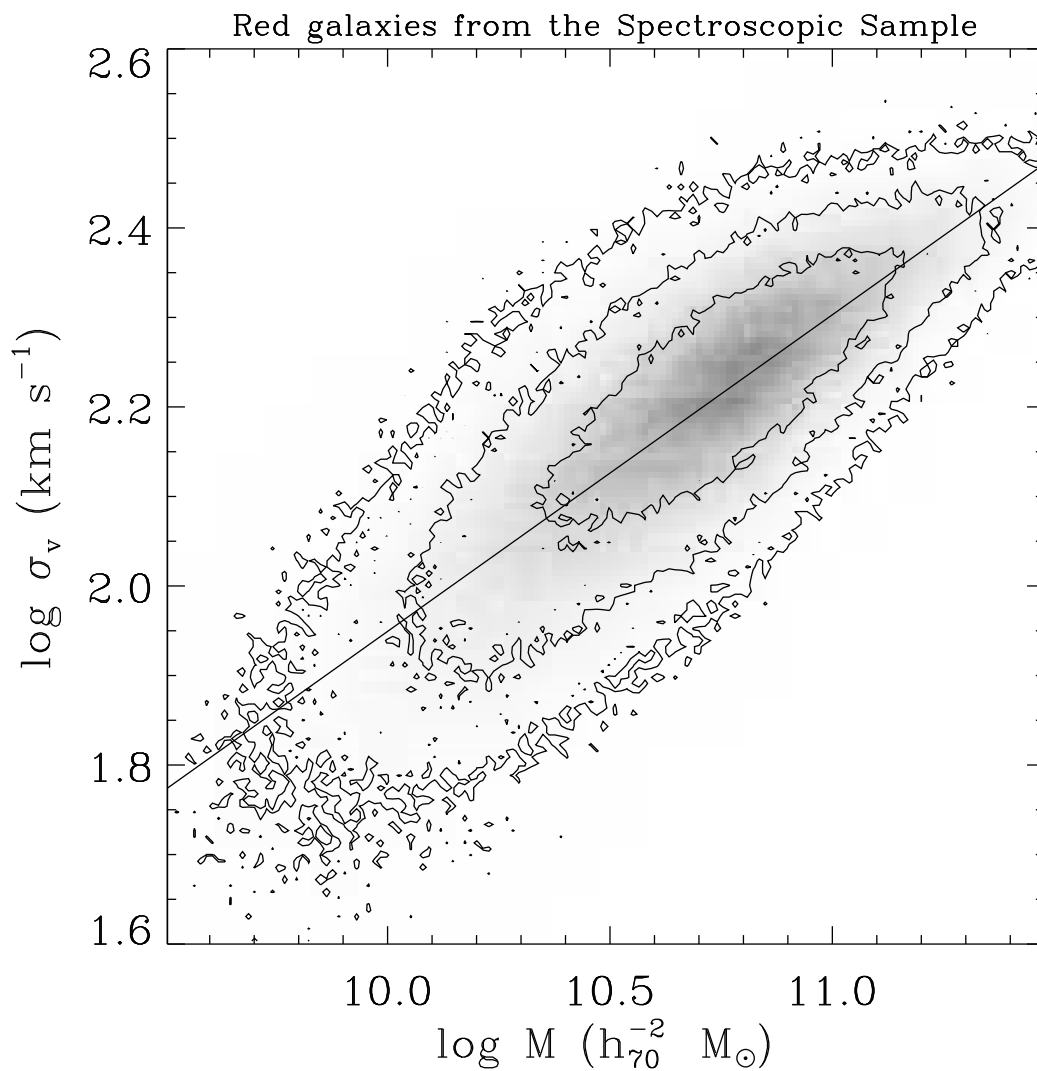


Fig. 9.— The relationship between σ_v , the stellar velocity dispersion and M , the stellar mass for red galaxies in the spectroscopic sample. The greyscale and the contours reflect the number of galaxies in each bin. The solid line is the linear fit, equation (6).

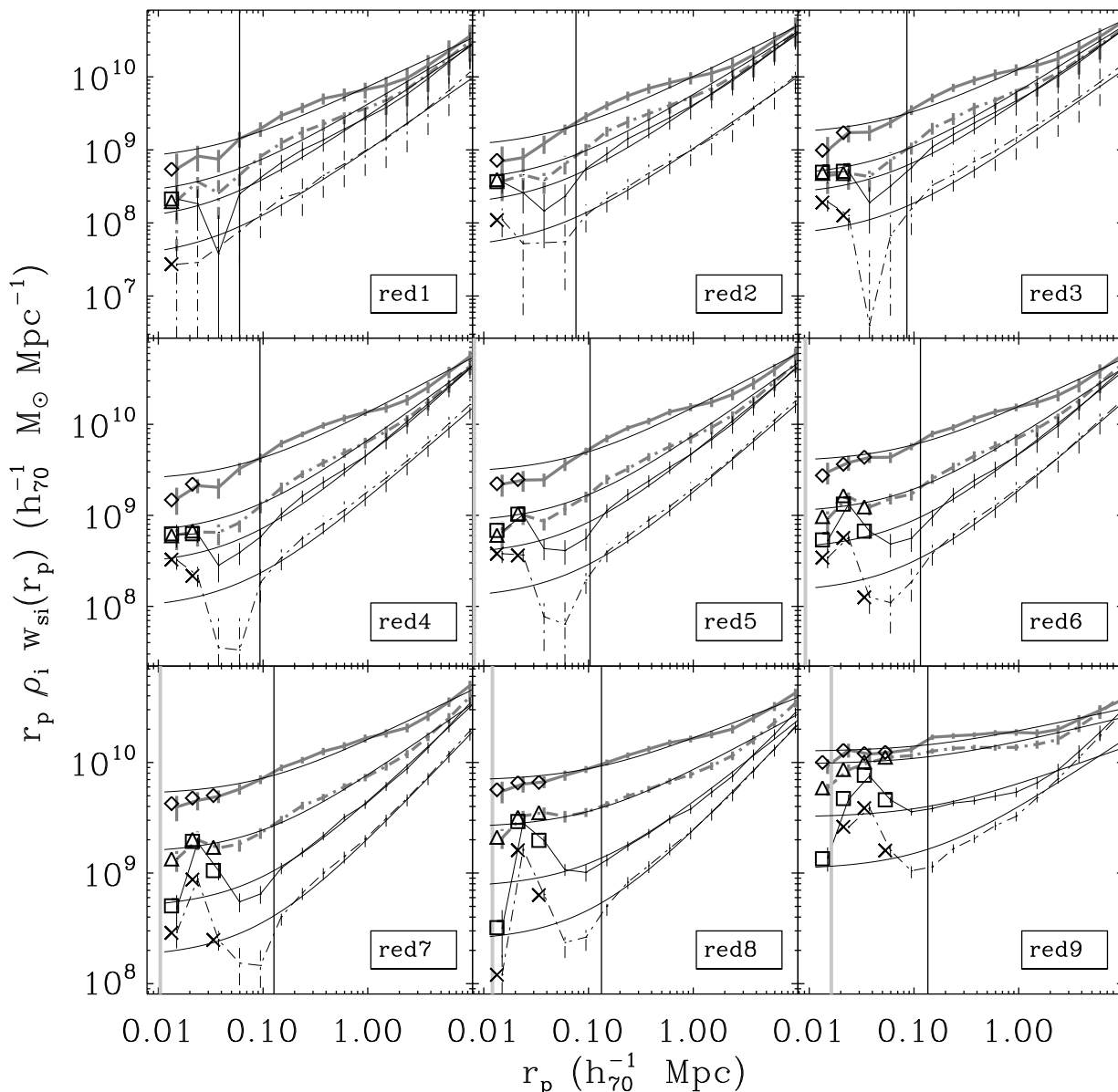


Fig. 10.— Projected two-dimensional cross-correlation functions $\rho_i w_p(r_p)$ between all of the 9 red spectroscopic subsamples and all red imaging subsamples, scaled by r_p for better illustration. The right vertical thin lines are corresponding to 55 arcsec at the median redshift of the spectroscopic galaxies, and the left vertical thick lines are corresponding to the median r_{90} for the spectroscopic galaxies. The error-bars are from the jackknife error covariance matrix only. All the lines show the results after photometry correction: the thick solid line shows imaging galaxies with $10^{-0.5} < M_i/M_s < 10^0$ (black diamonds are the result before photometry correction), the thick dashed line shows $10^{-1} < M_i/M_s < 10^{-0.5}$ (black triangles are the result before photometry correction), the thin solid line shows $10^{-1.5} < M_i/M_s < 10^{-1}$ (black squares are the result before photometry correction), and the thin dashed line shows $10^{-2} < M_i/M_s < 10^{-1.5}$ (black crosses are the result before photometry correction). The four curves are the fit lines(see text). The results before photometry correction are offset by 12% of our interval to the left.

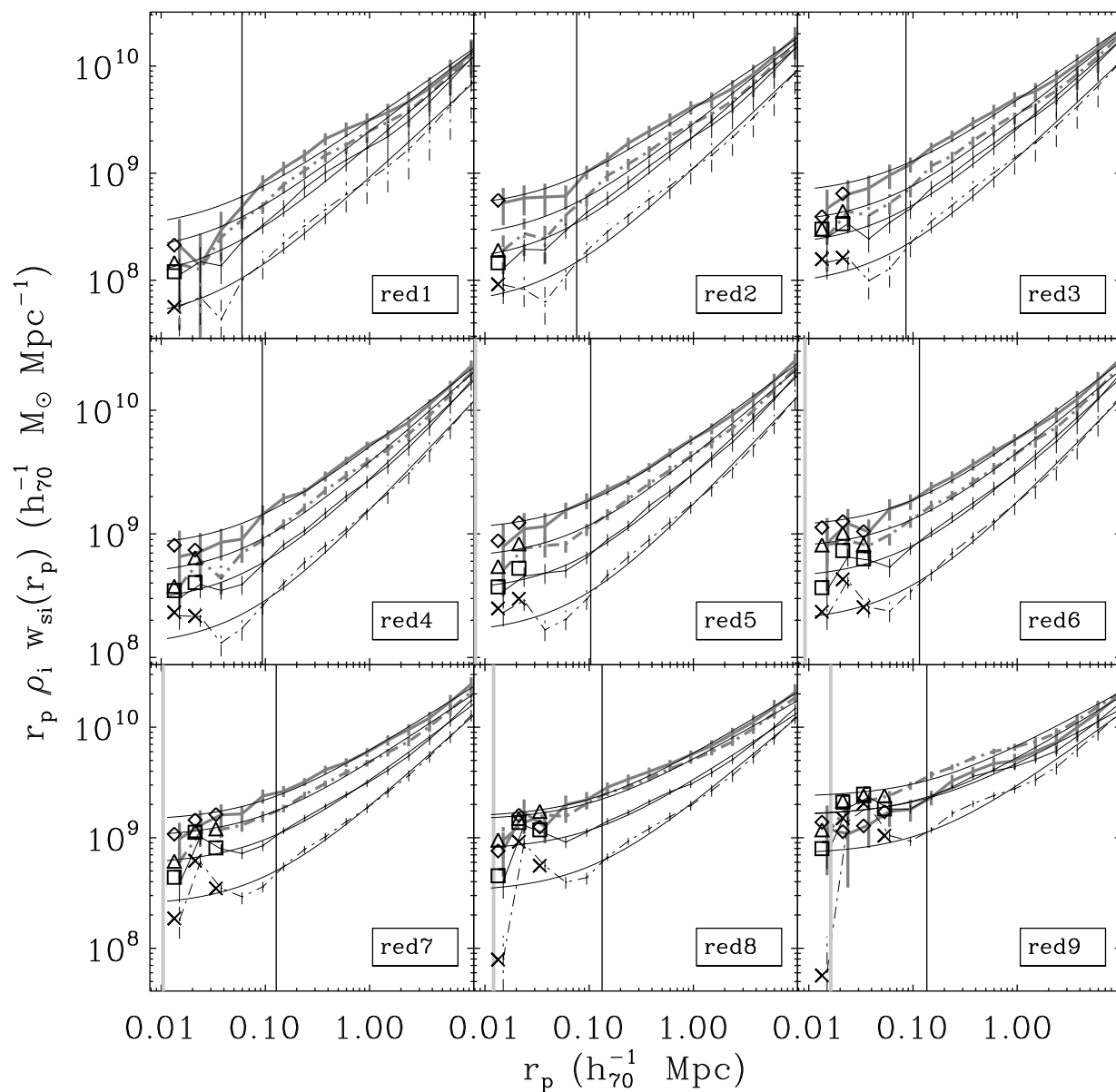


Fig. 11.— Same as Figure 10, but for the 9 red spectroscopic subsamples cross-correlated with all blue imaging subsamples.

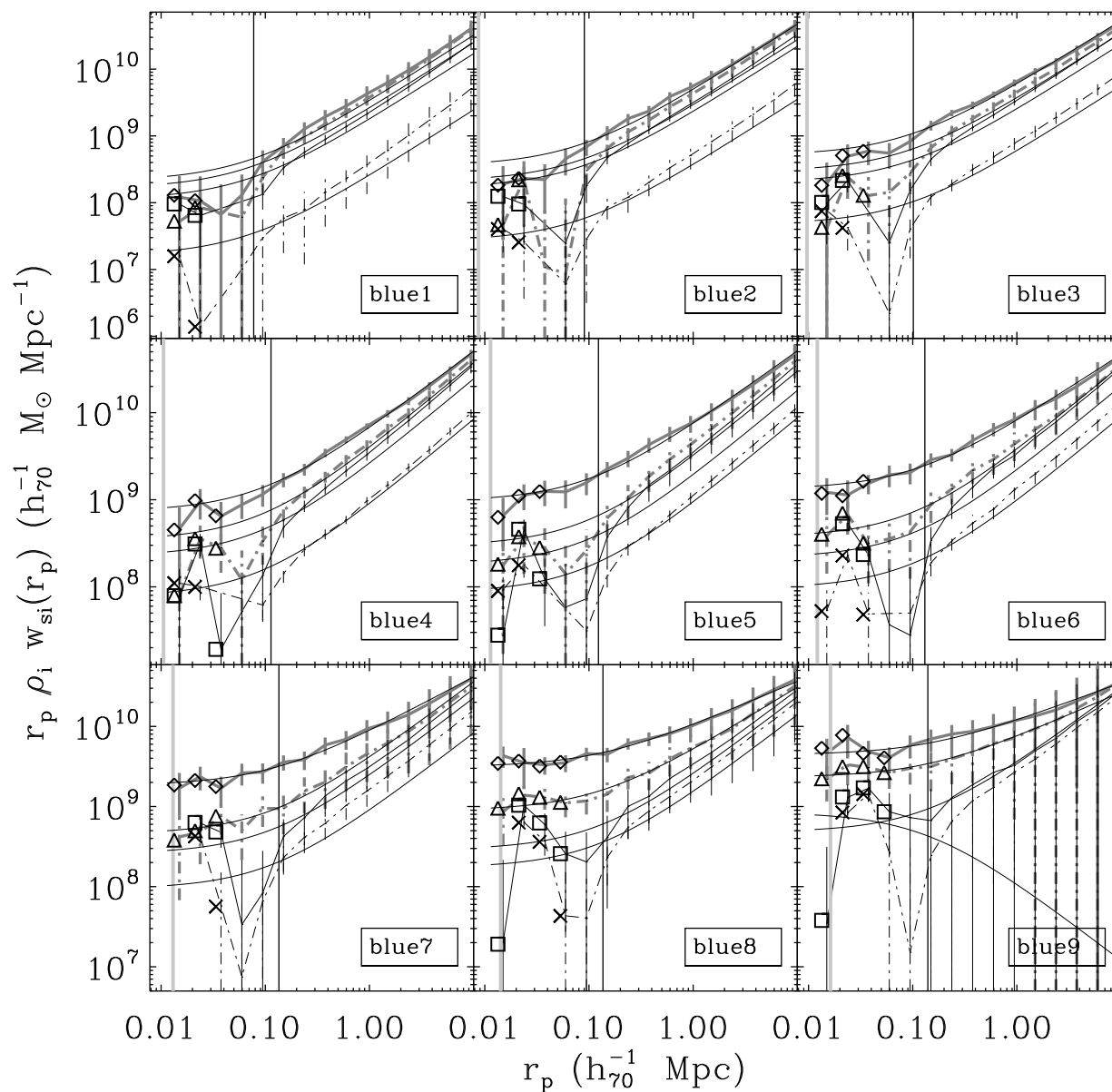


Fig. 12.— Same as Figure 10, but for the 9 blue spectroscopic subsamples cross-correlated with all red imaging subsamples.

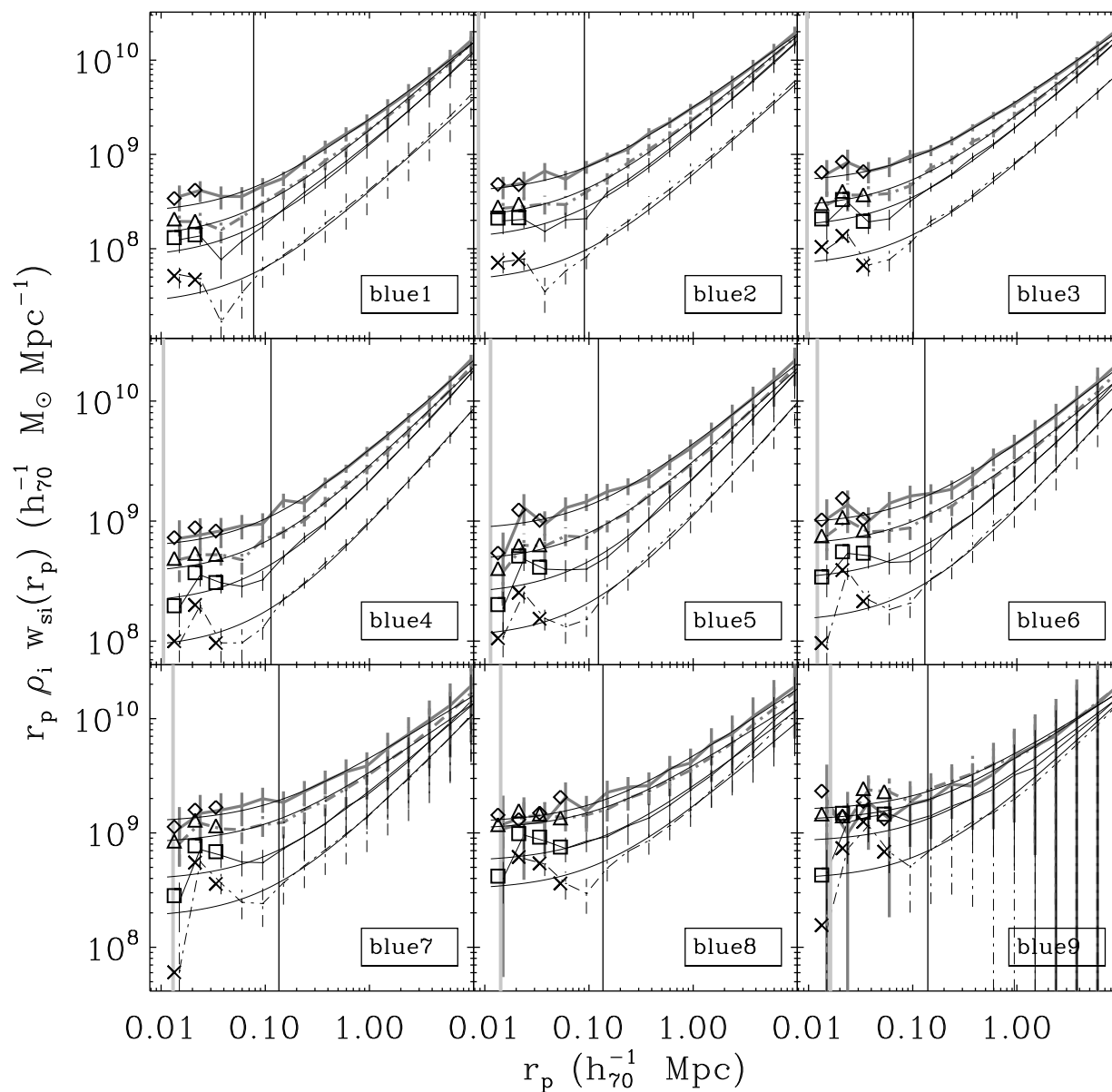


Fig. 13.— Same as Figure 10, but for the 9 blue spectroscopic subsamples cross-correlated with all blue imaging subsamples.

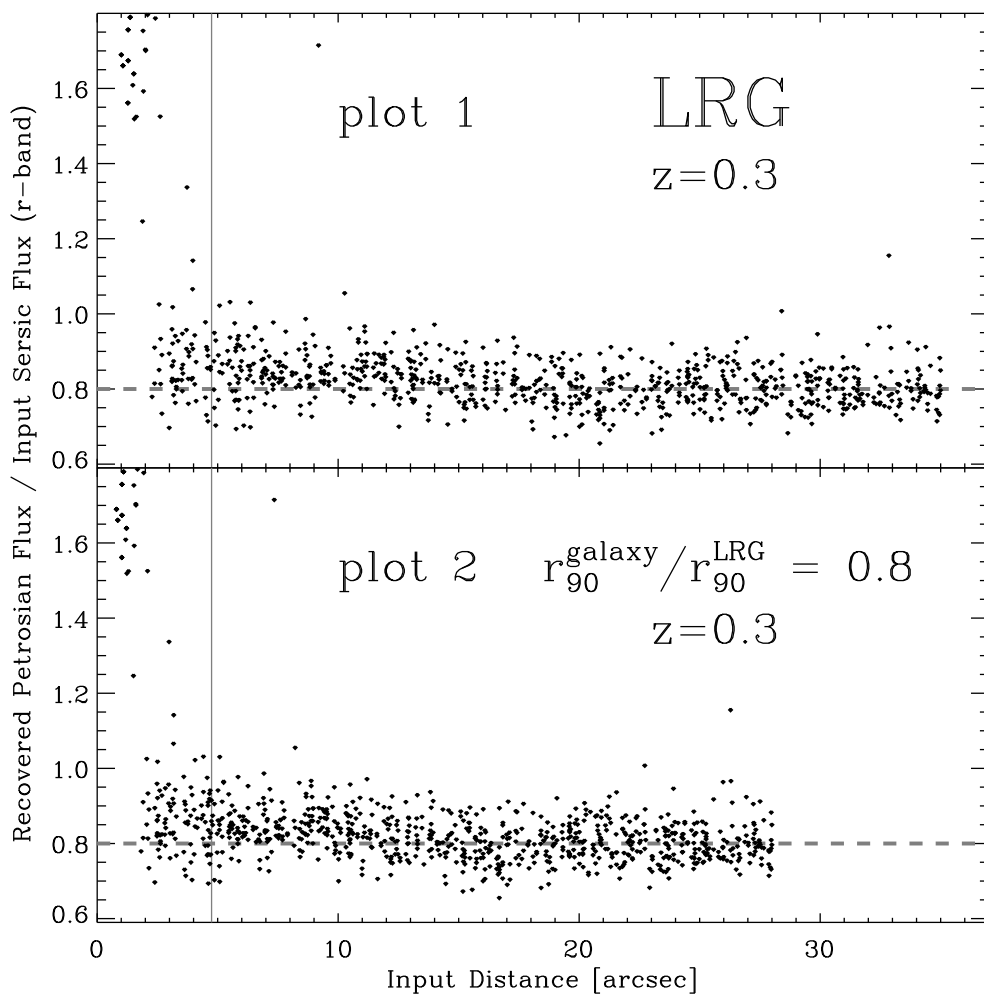


Fig. 14.— Recovered Petrosian flux to input Sérsic flux as a function of the separation of the two galaxies in the pair. We show both LRG and small galaxy whose radius is only 80% of that of LRG. The vertical line shows the smallest separation in our research at $z = .15$ and $r_p = 14.9h_{70}^{-1}$ kpc. For LRG, on average there is an excess in the recovered flux of galaxies separated by less than 20 arcsec.

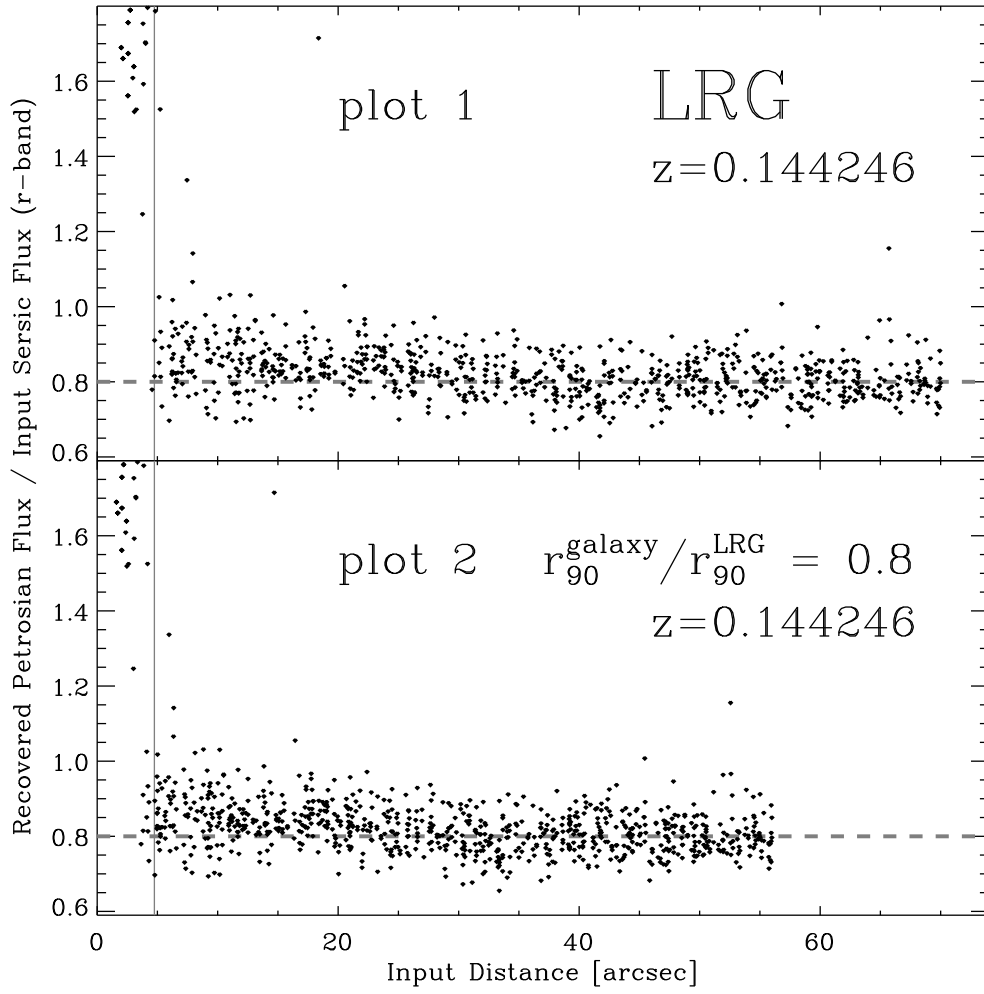


Fig. 15.— Recovered Petrosian flux similar as Figure 20.

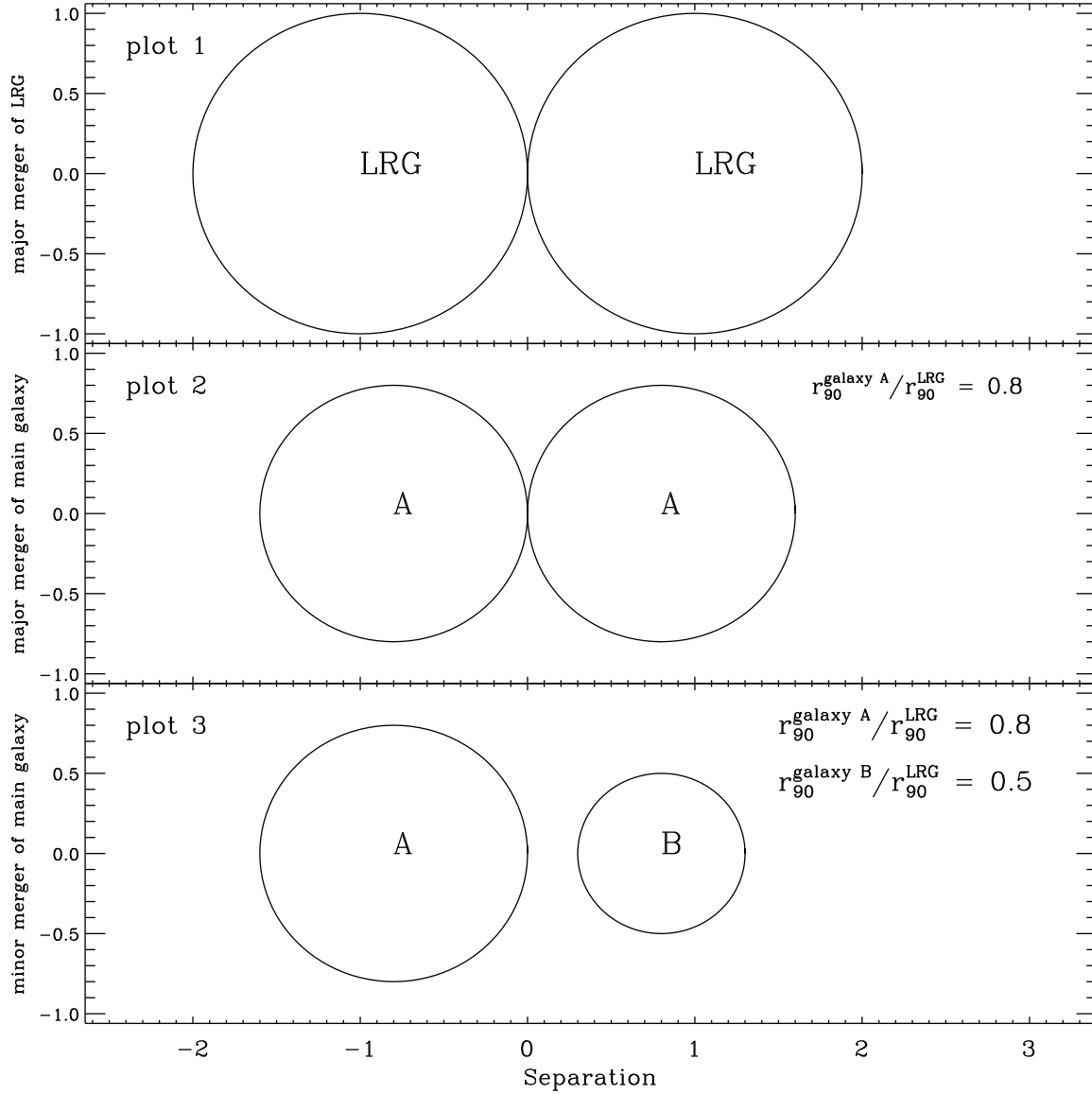


Fig. 16.— We show the major merger of LRG (Masjedi et al. 2006), major merger of main galaxy and minor merger of main galaxy. Please note that this is only a sketch, the radius and separation may be much different.

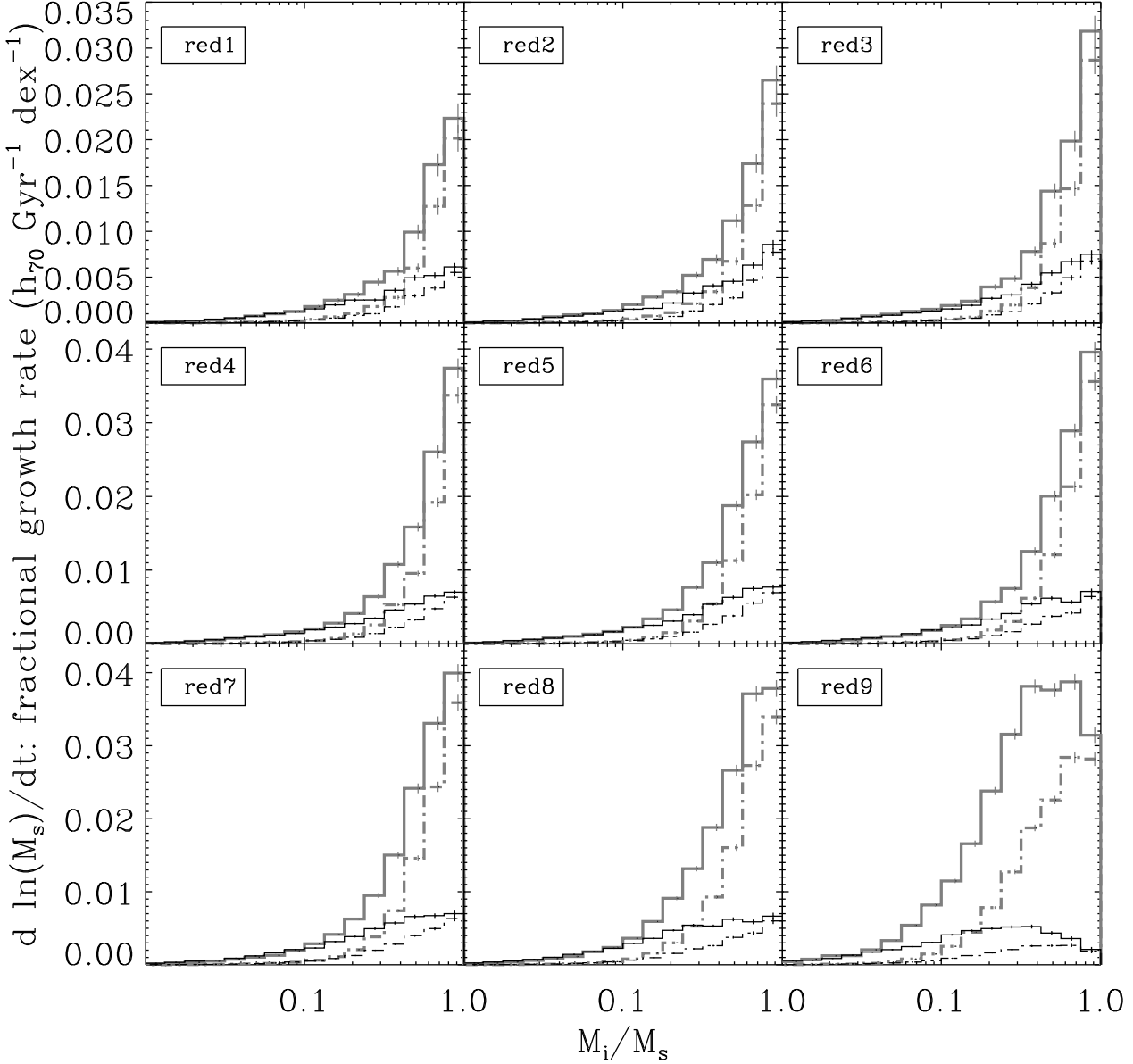


Fig. 17.— The mean fractional accretion rate for the 9 red spectroscopic subsamples $h_{70} \text{ Gyr}^{-1}$ per dex. The thick lines are for mergers with red galaxies from the imaging sample and the thin lines are for mergers with blue galaxies from the imaging sample. The solid lines are the merger rate under assumption of $t_{merge,i} = t_{KW,i}$, and the dashed lines are for the merger rate under assumption of $t_{merge,i} = t_{BT,i}$.

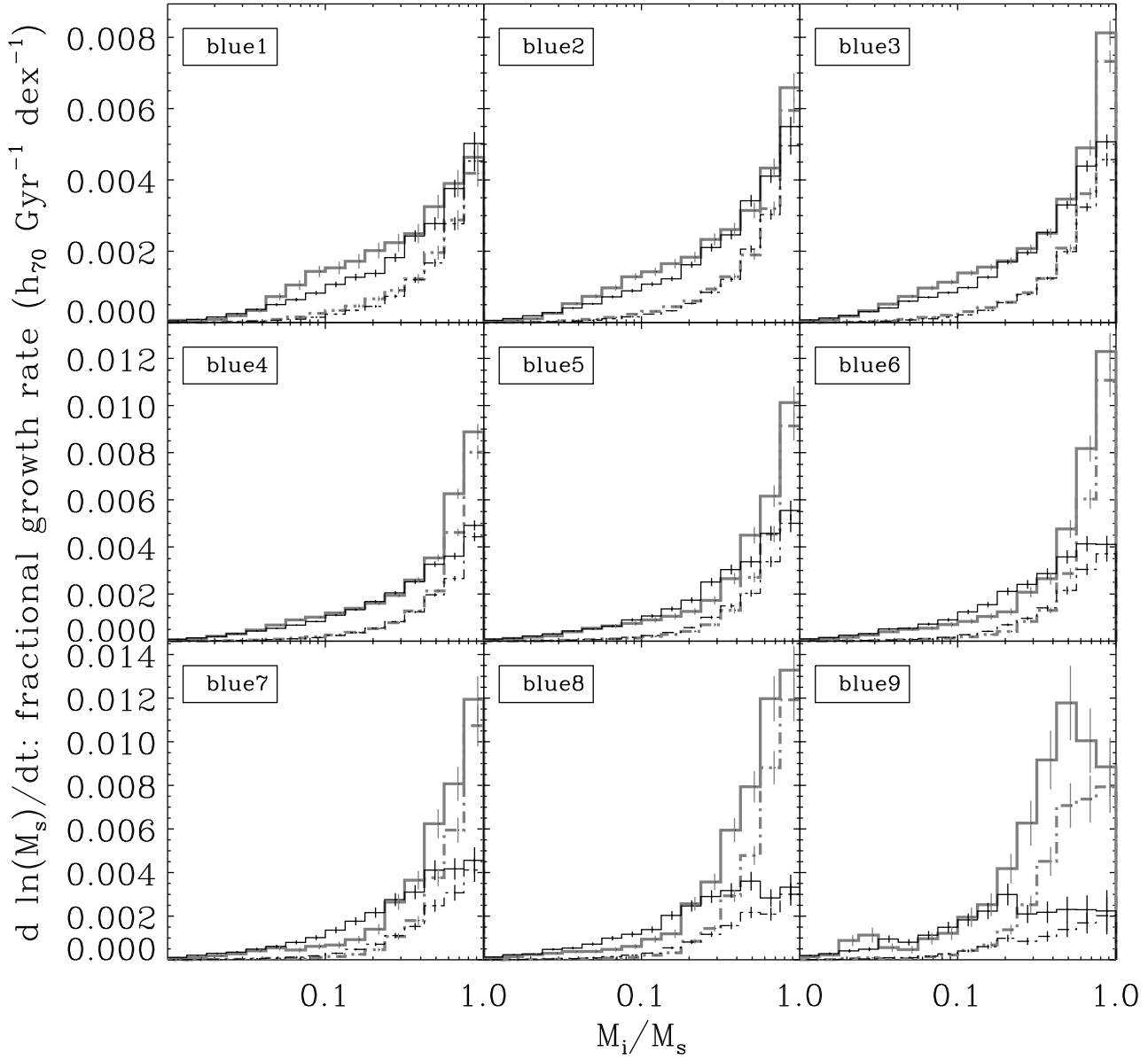


Fig. 18.— Same as Figure 17, but for the 9 blue spectroscopic subsamples.

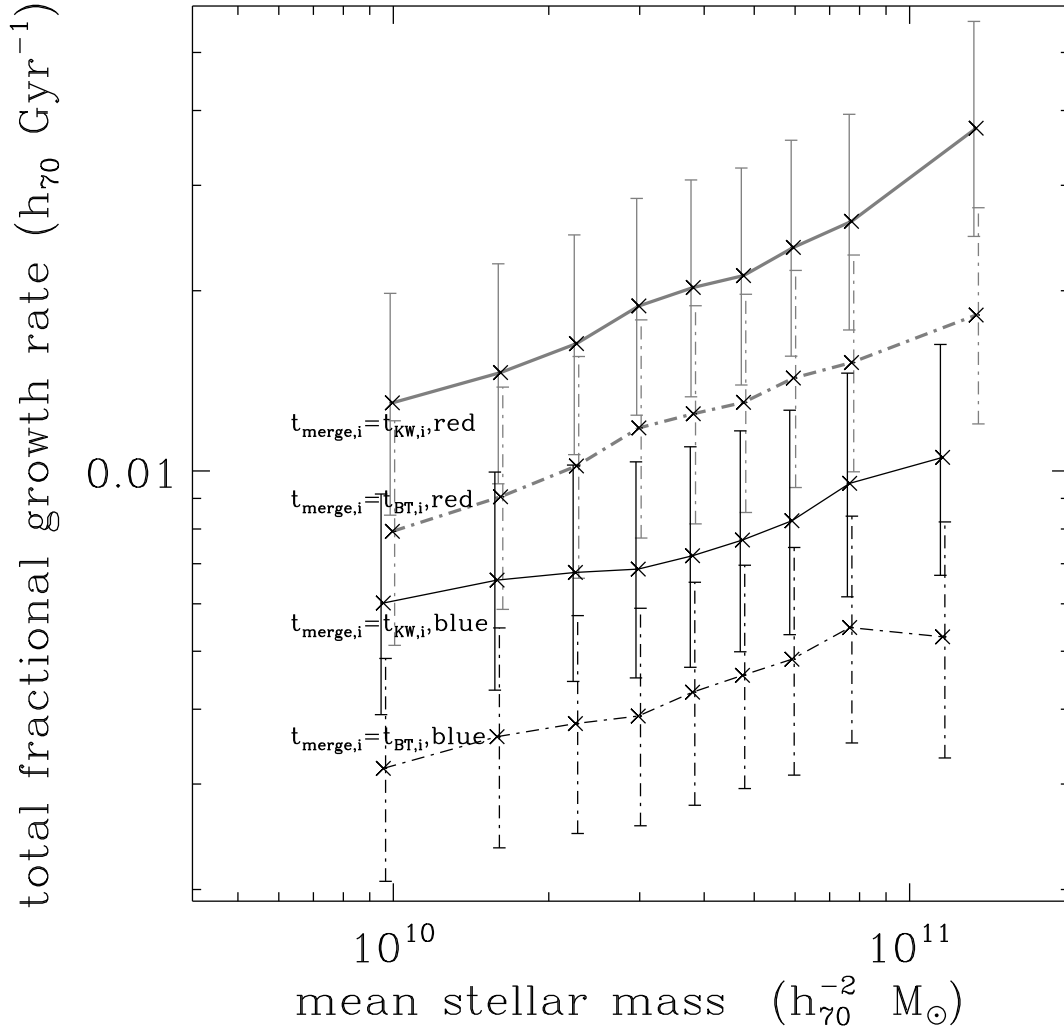


Fig. 19.— The total fractional accretion rates for each of the 18 spectroscopic subsamples $h_{70} \text{ Gyr}^{-1}$ integrating over all the galaxies from the imaging sample. The thick lines are for the red spectroscopic subsamples and the thin lines are for the blue spectroscopic subsamples. The solid lines are for the merger rate under assumption of $t_{\text{merge},i} = t_{\text{KW},i}$, and the dashed lines are for the merger rate under assumption of $t_{\text{merge},i} = t_{\text{BT},i}$.

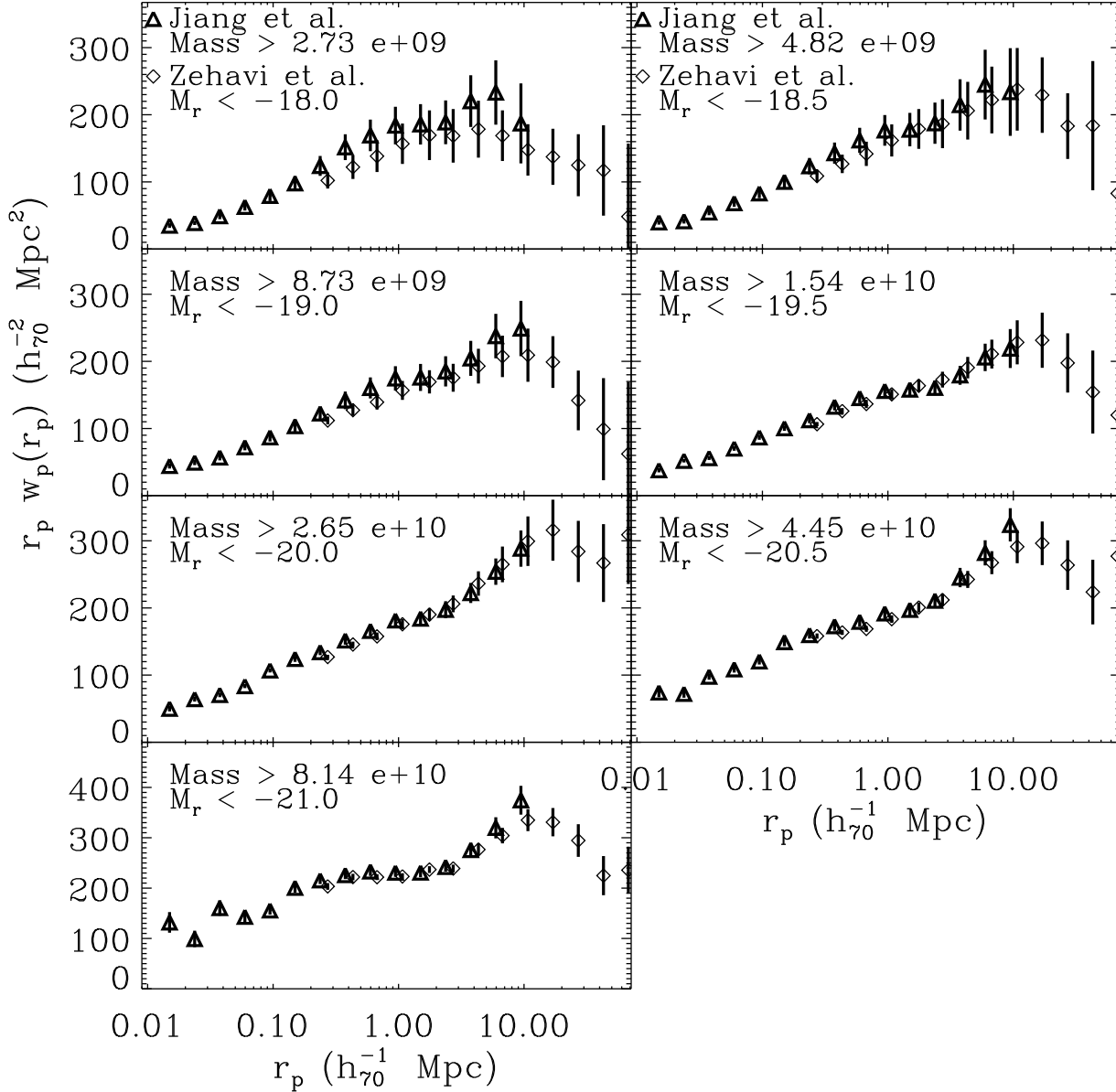


Fig. 20.— Projected correlation function $w_p(r_p)$ for the spectroscopic subsamples corresponding to mass-threshold samples as labeled, calculated as described in the text on small scales, combined with projected correlation function on intermediate scales from Zehavi et al. (2010). Please note that in order to compare these results easily, we offset the points of Zehavi et al. (2010) by 12% of our interval to the right.

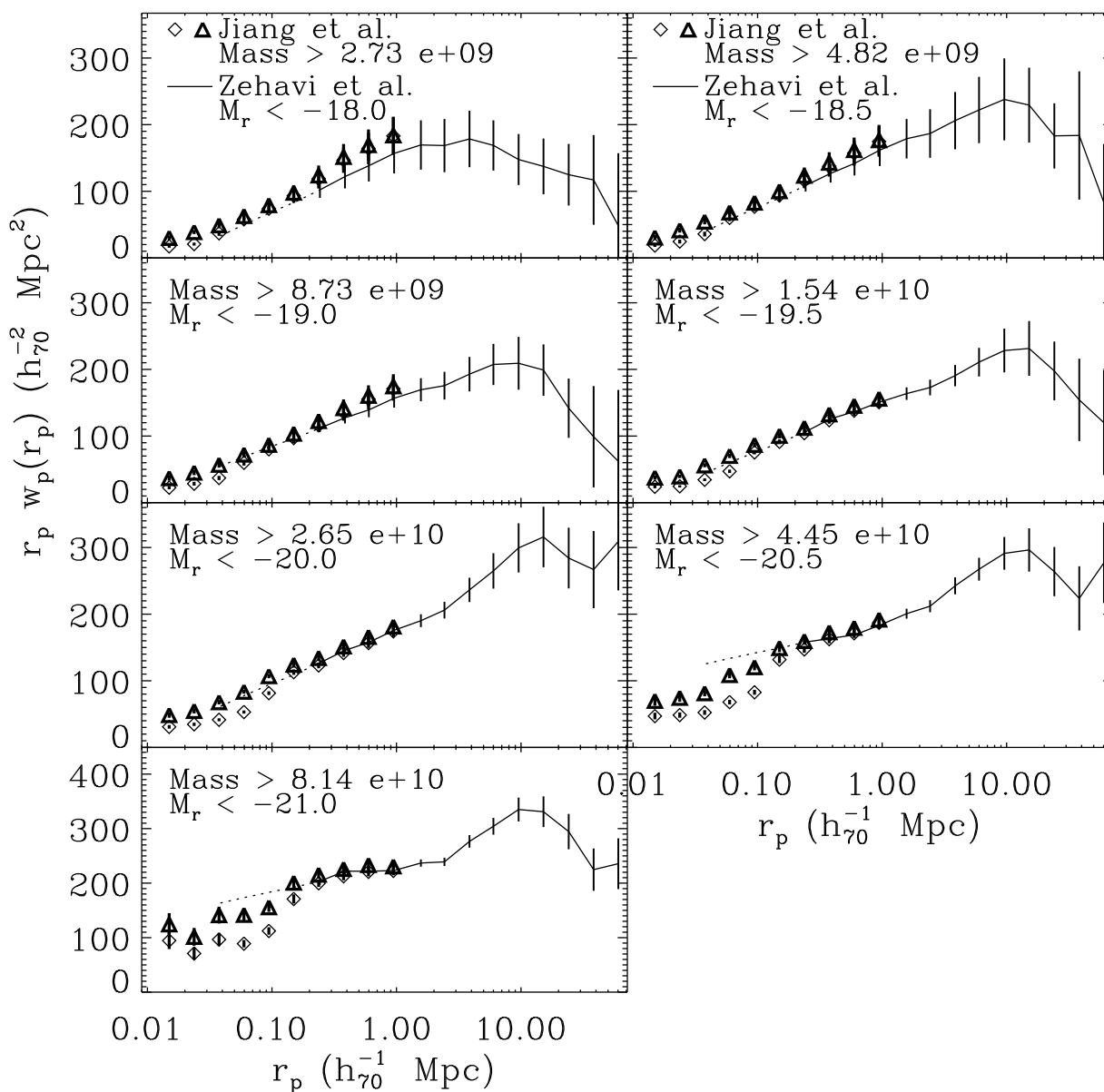


Fig. 21.— Projected correlation function $w_p(r_p)$ similar as Figure 20. There is no offset in this graph. The triangle points are our $w_p(r_p)$ with correction of fiber collisions, the diamond points are the $w_p(r_p)$ assuming $p_j = 1$ and $f_j = 1$, the solid lines with thin error bars are the $w_p(r_p)$ of Zehavi et al. (2010) and the dashed lines are the extension lines of Zehavi et al. (2010) described in the text. Please note that in order to compare these results easily, we only display our first ten data points.

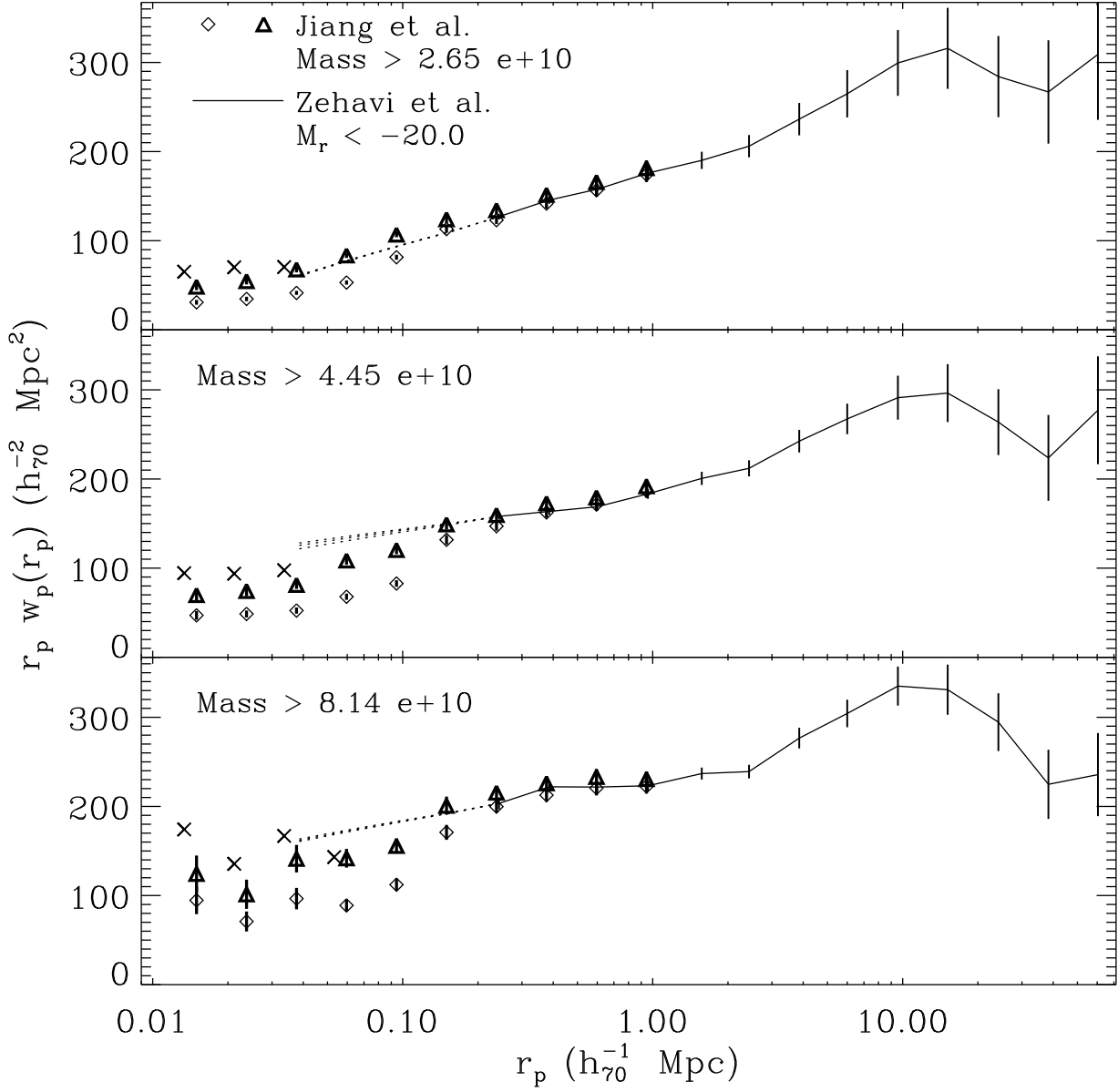


Fig. 22.— Projected correlation function $w_p(r_p)$ similar as Figure 21, but only display the last three plots. The black crosses in the second and third plots are our result before photometry correction which are offset by 12% of our interval to the left. Please note that the three extension dashed lines are fitting from the first five, first six and first seven data points of Zehavi et al. (2010).

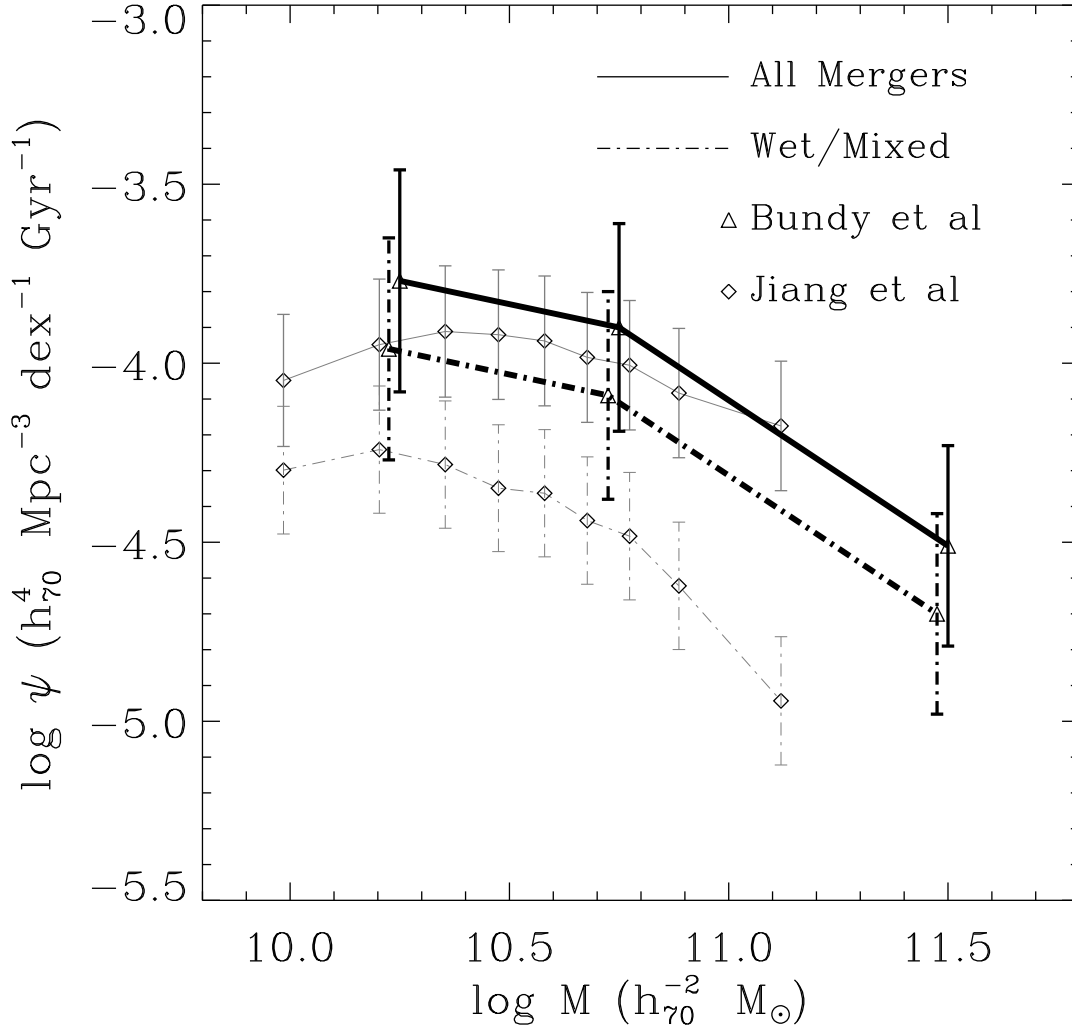


Fig. 23.— The comparison of our major merger rate MF at $0.03 < z < 0.15$ under assumption of $t_{merge} = t_{KW,i}$ with the major merger rate MF of Bundy et al. (2009) at $0.4 < z < 0.7$. Both of our mass ratios are $m/M > 0.25$. The open diamonds on the thick lines are our results, and the open triangles on the thin lines are the results of Bundy et al. (2009). The dashed lines show the results of excluding the approximate fraction of dry E/S0-E/S0 mergers, and the solid lines indicate the observed merger rate for all galaxies determined.

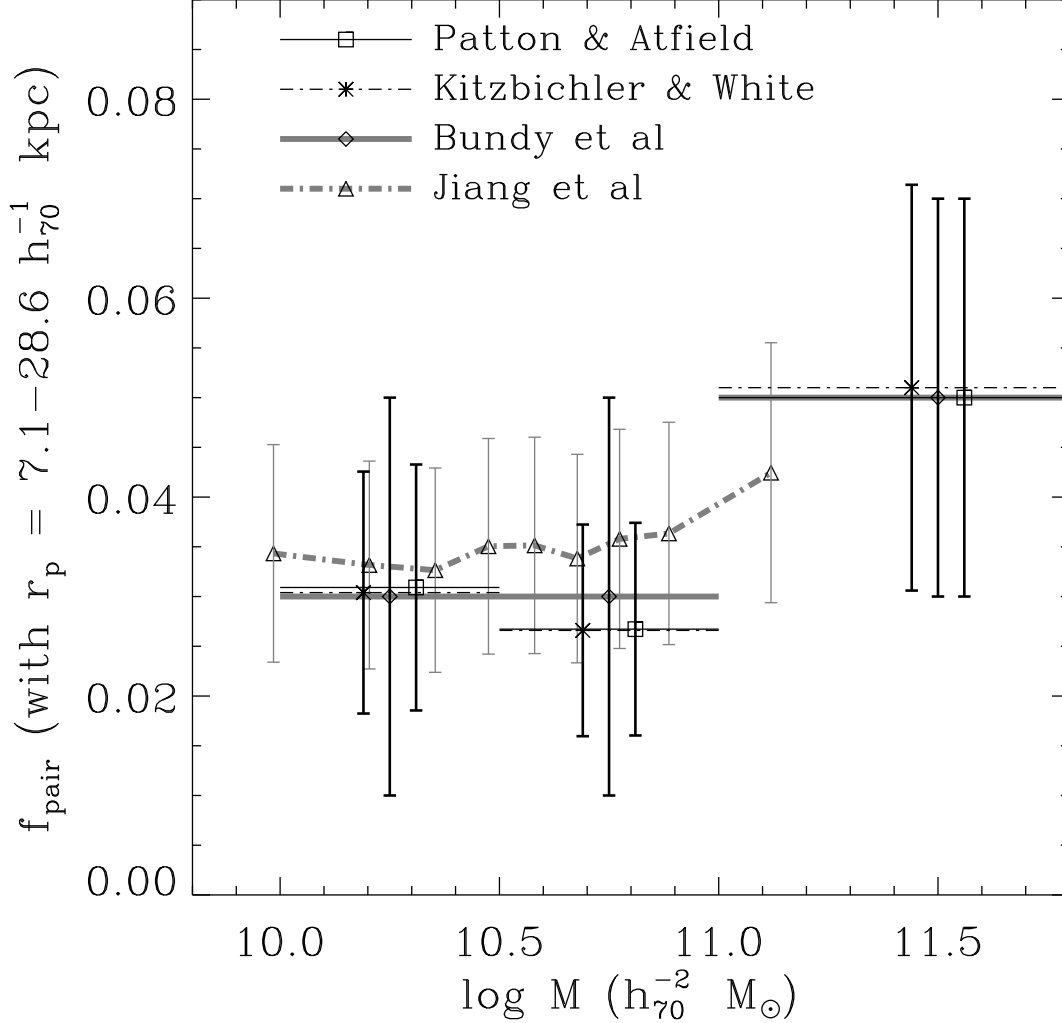


Fig. 24.— The comparison of our $f_{pair}^{7.1-28.6 h_{70}^{-1} \text{ kpc}}$ at $0.03 < z < 0.15$ with the $f_{pair}^{7.1-28.6 h_{70}^{-1} \text{ kpc}}$ of three recent results (Patton & Atfield 2008; Kitzbichler & White 2008; Bundy et al. 2009) at $0.4 < z < 0.7$. The open diamonds on the thick solid lines are the results of Bundy et al. (2009), and the open triangles on the thick dashed lines are our results. The thin horizontal solid lines show the results of Patton & Atfield (2008), and the thin horizontal dashed lines show the results of Kitzbichler & White (2008). Please note that the $f_{pairs}^{7.1-28.6 h_{70}^{-1} \text{ kpc}}$ of Patton & Atfield (2008) and Kitzbichler & White (2008) are calculated by $f_{pair} = R_{mg} \times T_{mg}/C_{mg}$.

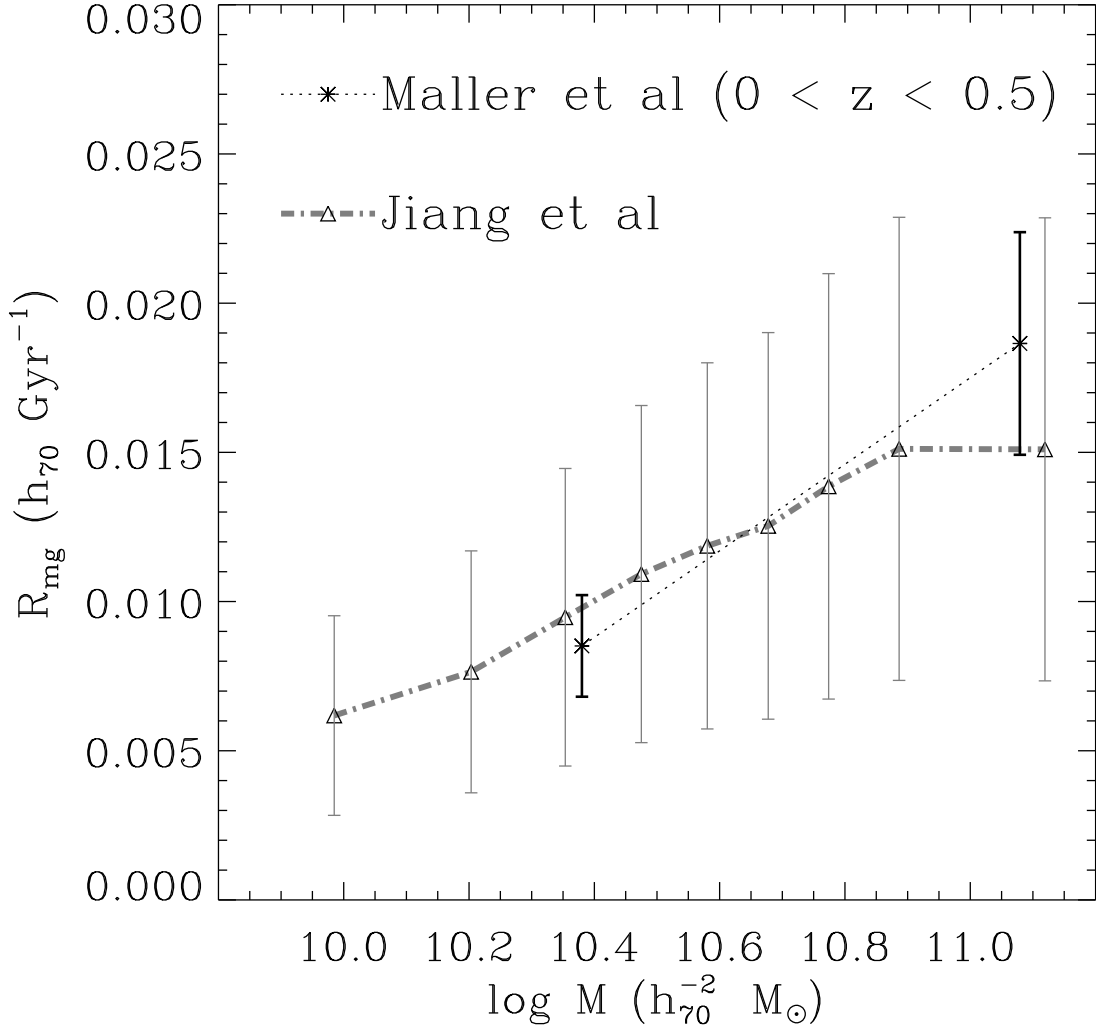


Fig. 25.— The comparison of our merger rates (per galaxy $h_{70} \text{ Gyr}^{-1}$) under assumption of $t_{\text{merge}} = t_{KW,i}$ at $0.03 < z < 0.15$ with the merger rates of Maller et al. (2006) at $0 < z < 0.5$. The open triangles on the dashed lines are our results, and the thin dotted lines are the best-fit result calculated from equation (5) of Maller et al. (2006). Both of our mass ratios are $m/M > 0.5$. Please note that the results of Maller et al. (2006) are estimated from a flat $\Omega_m = 0.4$ cosmology with $\sigma_8 = 0.8$, a Hubble constant $H_0 \equiv 100 h \text{ km s}^{-1} \text{ Mpc}^{-1}$ with $h = 0.65$, a baryon content $\Omega_b = 0.047$, and a spectral index $n = 0.93$. This difference of the two assumptions might lead the difference of the two slopes.

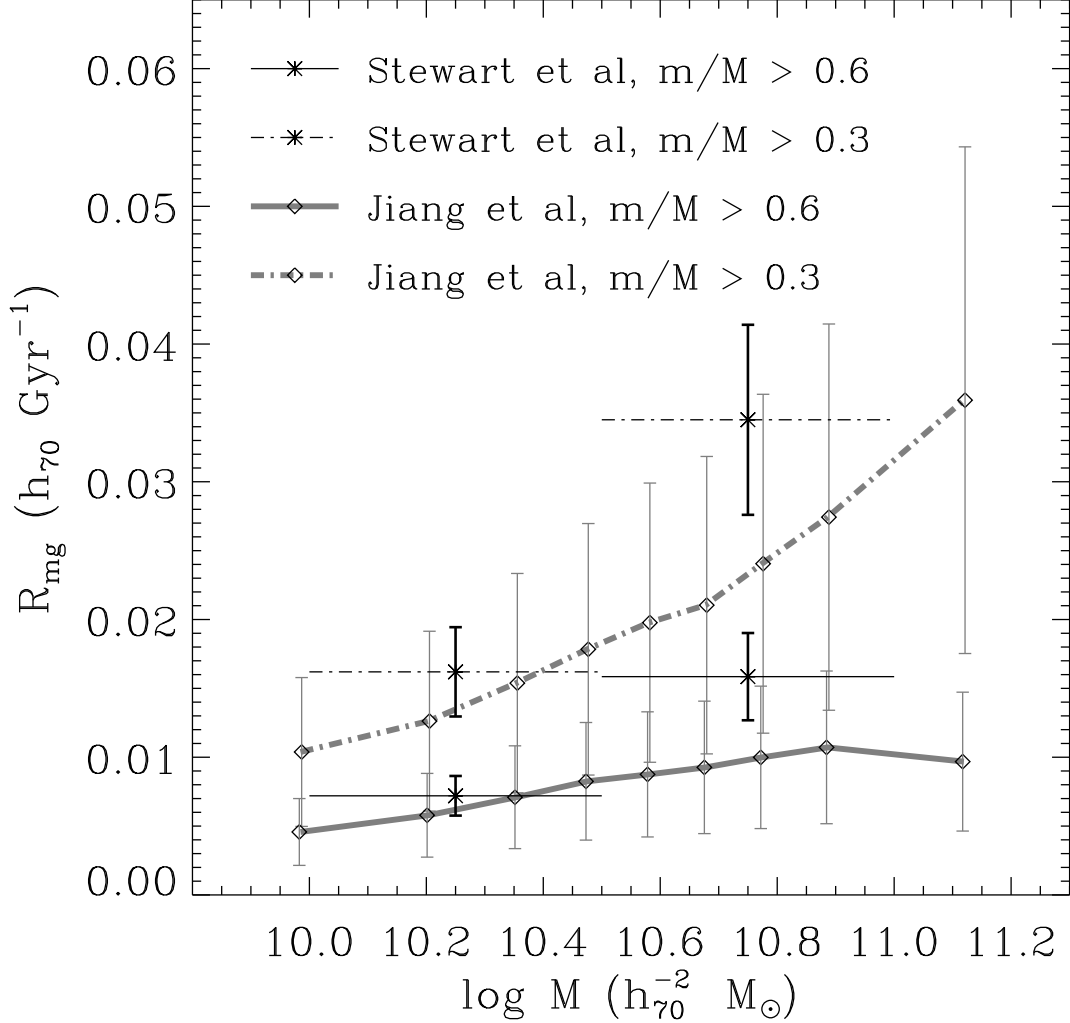


Fig. 26.— The comparison of our merger rates (per galaxy $h_{70} \text{ Gyr}^{-1}$) under assumption of $t_{\text{merge}} = t_{KW,i}$ at $0.03 < z < 0.15$ with the estimated merger rates calculated by the ‘Merger Rate Fitting Function’ of Stewart et al. (2009) at $z = 0.1$. The open diamonds on the thick lines are our results, and the horizontal thin lines are the best-fit results calculated from Table 1 of Stewart et al. (2009). The dashed lines show the results with mass ratios $m/M > 0.3$, and the solid lines show the results with mass ratios $m/M > 0.6$. Please note that the results of Stewart et al. (2009) are estimated from a flat $\Omega_m = 1 - \Omega_\Lambda = 0.3$ cosmology with a Hubble constant $H_0 \equiv 100 h \text{ km s}^{-1} \text{ Mpc}^{-1}$ and $h = 0.7$.